

Stabilized Co-Free Li-Rich Oxide Cathode Particles with An Artificial Surface Prereconstruction

Zhi Zhu, Rui Gao, Iradwikanari Waluyo, Yanhao Dong, Adrian Hunt, Jinhyuk Lee, and Ju Li*

Li-rich metal oxide (LXMO) cathodes have attracted intense interest for rechargeable batteries because of their high capacity above 250 mAh g⁻¹. However, the side effects of hybrid anion and cation redox (HACR) reactions, such as oxygen release and phase collapse that result from global oxygen migration (GOM), have prohibited the commercialization of LXMO. GOM not only destabilizes the oxygen sublattice in cycling, aggravating the well-known voltage fading, but also intensifies electrolyte decomposition and Mn dissolution, causing severe full-cell performance degradation. Herein, an artificial surface prereconstruction (ASR) for Li_{1.2}Mn_{0.6}Ni_{0.2}O₂ particles with a molten-molybdate leaching is conducted, which creates a crystal-dense anion-redox-free LiMn_{1.5}Ni_{0.5}O₄ shell that completely encloses the LXMO lattice (ASR-LXMO). Differential electrochemical mass spectroscopy and soft X-ray absorption spectroscopy analyses demonstrate that GOM is shut down in cycling, which not only stabilizes HACR in ASR-LXMO, but also mitigates the electrolyte decomposition and Mn dissolution. ASR-LXMO displays greatly stabilized cycling performance as it retains 237.4 mAh g⁻¹ with an average discharge voltage of 3.30 V after 200 cycles. More crucially, while the pristine LXMO cycling cannot survive 90 cycles in a pouch full-cell matched with a commercial graphite anode and lean (2 g A⁻¹ h⁻¹) electrolyte, ASR-LXMO shows high capacity retention of 76% after 125 cycles in full-cell cycling.

than a decade. In LXMO with heavy Li_{ML} substitution ($X = 0.2$), less than half of the capacity comes from M cation redox (e.g., Ni^{2+/4+}, Co^{3+/4+}, etc.), while the major capacity is contributed from oxygen anion redox ($O^{2-} \leftrightarrow O^{\alpha-}$, $\alpha < 2$).^[2–5] Therefore, the high capacity of LXMO originates from heavy hybrid anion- and cation-redox (HACR) behaviors with high oxygen oxidation during cycling.^[6] However, HACR is a double-edged sword: while contributing to a high capacity at high voltage from anion redox is certainly wonderful, because of the decreased electrostatic force and ionic radius, the highly oxidized O^{α-} ions would also become mobile at high voltage. It has been reported that while the migration barrier of O²⁻ is above 2.4 eV in LXMO, that of the oxidized O^{α-} species can decrease to below 0.9 eV.^[7] The much-increased oxygen mobility at room-temperature (RT) would cause enhanced oxygen migration (OM) in the lattice.

OM can be local or global. While local oxygen migration (LOM) refers to adjustments of oxygen positions within a short length scale around the original sites, depending on the local chemical environ-

ment,^[8] global oxygen migration (GOM) refers to the scenario in which oxygen ions can diffuse a long distance towards the particle surface until they reach surface and escape from the particle. GOM accounts for the well-known oxygen loss when charging LXMO, as widely reported in the literature.^[9,10] Oxygen loss reduces the average M valence (as oxygen O^{α-} leaves, it has to leave behind the $-\alpha e$ charge) and leads to an excess M reduction (e.g., Mn⁴⁺ → Mn³⁺) in the subsequent lithiation, shifting the HACR behavior by increasing the proportion of cation redox (lower voltage) at the expense of anion redox (higher voltage) in the following cycles,^[2] and aggravating the cyclic voltage fading.


The haphazard exit of oxygen also destabilizes the lattice structure, and tends to trigger irreversible phase transformations (IPT), and immediately increases the impedance in cycling.^[11] While charging, the surface of LXMO particle always delithiates more than the bulk to bleed the Li ions in the core, so the oxygen ions at the particle surface are always overoxidized, becoming more mobile and easier to escape from the lattice. Thus GOM and IPT always start from the particle surface (Figure 1b), and here we can term this IPT process as a “natural surface reconstruction (NSR).” Because NSR happens in

1. Introduction

The layered Li-rich oxide material, with formula of Li_{1+x}M_{1-x}O₂ (LXMO, M = Mn and Co or Ni, etc.), is the most likely candidate for next-generation cathode materials for Li ion battery due to the high energy density above 900 Wh kg⁻¹ (vs Li anode).^[1] However, LXMO suffers from serious voltage/capacity fading in cycling, which has prevented its commercialization for more

Dr. Z. Zhu, Dr. R. Gao, Dr. Y. Dong, Dr. J. Lee, Prof. J. Li
Department of Nuclear Science and Engineering
and Department of Materials Science and Engineering
Massachusetts Institute of Technology
Cambridge, MA 02139, USA
E-mail: liju@mit.edu

Dr. I. Waluyo, Dr. A. Hunt
National Synchrotron Light Source II
Brookhaven National Laboratory
Upton, NY 11973, USA

 The ORCID identification number(s) for the author(s) of this article can be found under <https://doi.org/10.1002/aenm.202001120>.

DOI: 10.1002/aenm.202001120

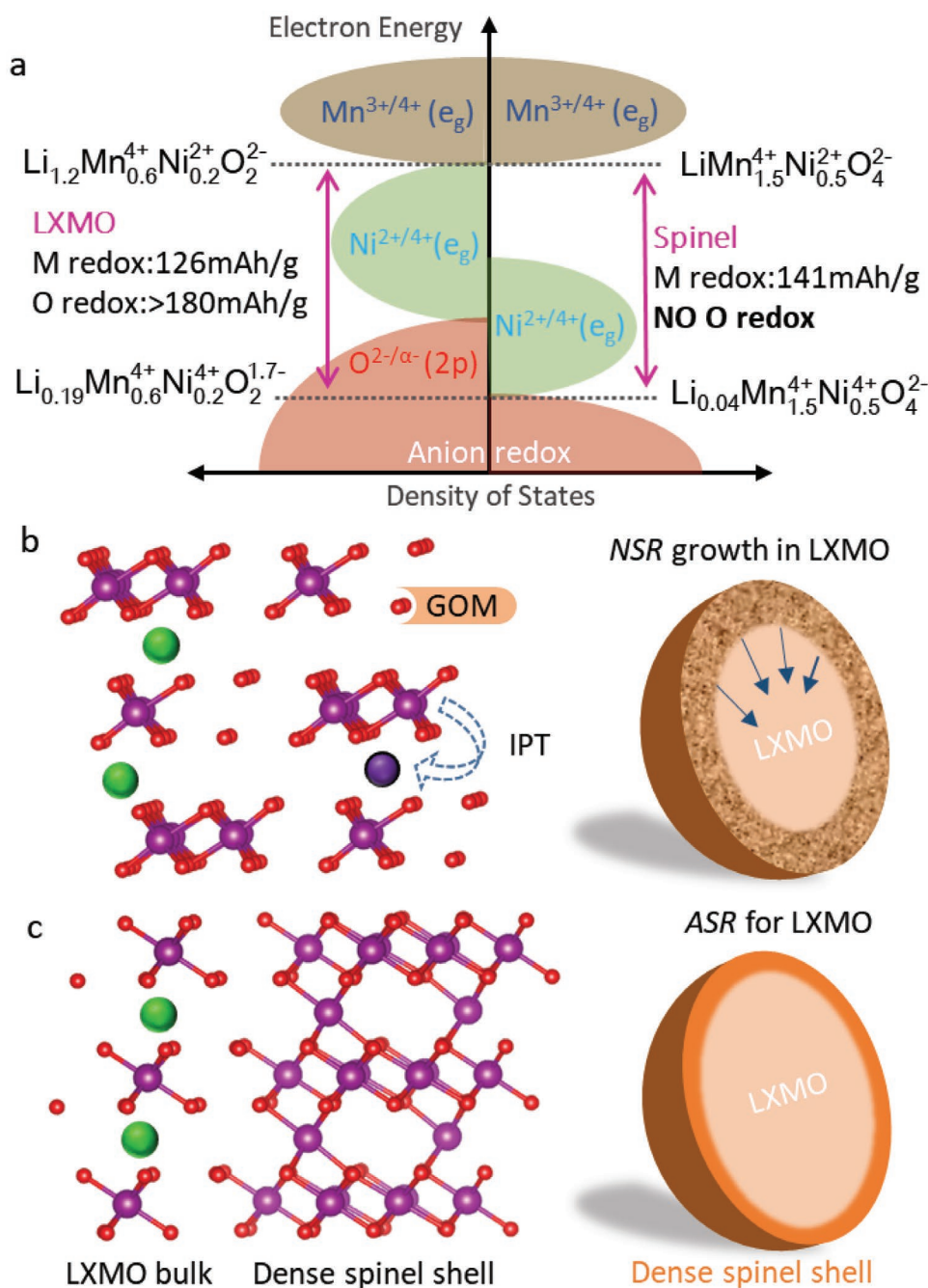


Figure 1. Electronic bands, lattice structures and schematic particles of the pristine LXMO (P-LXMO) and ASR conducted LXMO (ASR-LXMO). a) The band structures in LXMO ($\text{Li}_{1.2}\text{Mn}_{0.6}\text{Ni}_{0.2}\text{O}_2$) and spinel $\text{LiMn}_{1.5}\text{Ni}_{0.5}\text{O}_4$, and the Fermi levels at charge and discharge states, showing the capacity contributions from M cation redox and O anion redox when initially charging the two phases. b) The schematic of GOM and IPT in the fully charged P-LXMO lattice and the continuous NSR growth in the P-LXMO particle in cycling. c) The schematic fully charged lattice of the conceived ASR-LXMO particle and the stable phase in cycling. The green, violet and red balls in (b) and (c) represent Li, M (Ni/Mn), and O ions.

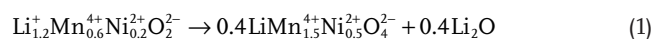
room-temperature cycling, it is hard to reconstruct into a dense crystal. With rampant GOM and oxygen release, NSR is likely uncontrollable, and prefers to produce oxygen vacancies and lattice flaws, like a rout instead of an ordered retreat. In other words NSR is not self-sealing or self-passivating, and the produced flaws (e.g., boundaries, dislocations) further “infect” the interior of the particle and facilitate GOM, with NSR penetrating into the deep bulk (Figure 1b). Wang and co-workers^[12] reported

that, in cycling, massive oxygen voids were generated from the LXMO particle surface, then gradually injected throughout the whole particle in 200 cycles. The continuous GOM also promotes the carbonate–electrolyte decomposition,^[13–15] while the Mn^{3+} ions aggravate Mn dissolution from the cathode and deposition at the anode,^[16–19] both of which would seriously degrade the cycling performance, especially in a practical full-cell matching with graphite anode and lean electrolyte.^[18,20,21]

In industrial cells, the amount of electrolyte used is only 1.5–3 g A⁻¹ h⁻¹,^[22,23] and this total amount of liquid electrolyte needs to form stable SEI at the anode side and CEI at the cathode side, and wet cathode pores, anode pores and separator, so additional side reactions with the liquid electrolyte (especially those that generate gases^[24]) will be extremely harmful to the full-cell cycling. Therefore, enabling HACR but stopping oxygen release and NSR is the key to developing a stable cyclic LXMO cathode with high energy density. Coatings were attempted in literatures,^[25,26] but these foreign coatings tend to form islands instead of a contiguous passivation shell on the particle surface, which can hardly prevent GOM and NSR in a long cycling.

Though NSR is not self-sealing in cycling, IPT transforms the LXMO lattice to a thermodynamically more stable phase at high voltage (e.g., layered → spinel/rock salt). So, if we can eliminate the oxygen vacancies and defects from the early NSR, creating an integral crystal dense shell to cover the interior LXMO bulk, then the shell will not only remain thermodynamically stable in battery cycling, but also seal the core and stop further GOM from occurring in the particle (Figure 1c), thereby enhancing cycling stability. Therefore, in this work, unlike the additive process of foreign coatings, we performed a subtractive process on the Li_{1.2}Mn_{0.6}Ni_{0.2}O₂ particles with leaching and annealing by molten salt. Thanks to the high temperature annealing, this artificial surface preconstruction (ASR) created a crystal-dense spinel shell at the Co-free Li_{1.2}Mn_{0.6}Ni_{0.2}O₂ particle surface. As the cost of Co raw-material is 2–3× that of Ni, and 20× that of Mn, this Co-free and Ni-lean Li_{1.2}Mn_{0.6}Ni_{0.2}O₂ is much cheaper than industrial mainstays like LiCoO₂ and Ni-rich oxides,^[27] and thus could be suitable for both consumer electronics and automotive batteries, provided that the two well-known challenges can be overcome: a) voltage fading and cycling instability, especially in lean electrolyte conditions like 2 g (electrolyte) A⁻¹ h⁻¹, and b) Mn dissolution into the electrolyte that destroys the graphite anode and also causes the electrolyte to continuously decompose.^[16]

Instead of electrochemical Li⁺ extraction in room-temperature cycling (NSR), we quantitatively “expel” some Li₂O from the Li_{1.2}Mn_{0.6}Ni_{0.2}O₂ particle surface through a chemical leaching at 750 °C, which reconstructs the surface to be a LiMn_{1.5}Ni_{0.5}O₄ spinel shell



LiMn_{1.5}Ni_{0.5}O₄ is a well-known 5 V class high-voltage cathode.^[28] Though the surface transforms to a spinel phase after ASR, it still takes high lattice coherence with the LXMO bulk, as the two phases share the same oxygen sublattice.^[29–31] Crucially, the high-temperature ASR anneals out the Li/O vacancies as well as the dislocations,^[11,32,33] which were always produced in NSR, making the artificially created spinel shell crystal-dense.

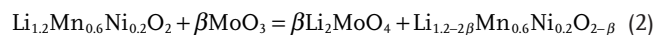
Therefore, the LXMO particles after ASR (ASR-LXMO) can achieve the following unique functions when charged up to 4.8 V versus Li⁺/Li: 1) as Figure 1c shows, in the Li_{1.2}Mn_{0.6}Ni_{0.2}O₂ bulk, with more than 90% in volume, O anion redox contributes more than 50% capacity to achieve a super-high capacity. Though the LiMn_{1.5}Ni_{0.5}O₄ spinel shell discharges less capacity (Figure 1a) when charged to 4.8 V,^[34–36] it does not entail anion redox, O^{α-} and enhanced oxygen mobility.^[37] Therefore, in the ASR-LXMO cycling, only the O²⁻ ions in the Li_{1.2}Mn_{0.6}Ni_{0.2}O₂

bulk can be highly oxidized and become mobile (like the concept of “solid oxygen” anion redox^[38,39]), but they are fully enclosed in the particle bulk and cannot trespass the dense spinel shell, so that GOM can be completely stopped within the particles, promoting strongly stabilized HACR behavior and thus stabilizing the working voltage in cycling. As the oxygen release detrimental to room-temperature cycling is pre-empted by the high-temperature Li₂O extraction and structural annealing, ASR can be considered to be a “preimmunization” process for LXMO particles against future GOM and NSR in the cell cycling. 2) The stopped GOM can stabilize the Mn valence at +4 in cycling, so the elimination of Mn³⁺ ions, which were always produced in the pristine LXMO (P-LXMO) cycling, would greatly prevent Mn dissolution and improve cycling stability, especially of the full-cell with graphite anode.^[40] 3) The prevented GOM can also make ASR-LXMO particles much more friendly to work with the carbonate electrolyte, which always decomposed when oxygen escaped from the cathode.^[9,41] So in this work, we will show a much-enhanced cycling stability of ASR-LXMO in a full-cell that matched with commercial graphite anode and lean electrolyte (2 g A⁻¹ h⁻¹). Combining such high performance with its cheap raw material cost (estimated to be <1/5 of LiCoO₂), ASR-LXMO presents an attractive option of cathode material for both consumer electronics and automotive batteries.

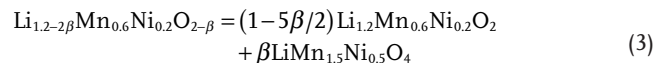
2. Results and Discussion

2.1. Artificial Surface Preconstruction for Li_{1.2}Mn_{0.6}Ni_{0.2}O₂ Particles

We have previously developed a high-temperature Li-O leaching method by molten molybdate treatment and successfully established a gradient Li/M concentration at a Co-containing Li-rich crystal surface.^[42] In this work, we used an optimized molten molybdate leaching (Equation (2)) at 750 °C for ASR to create a dense spinel shell for Li_{1.2}Mn_{0.6}Ni_{0.2}O₂ particle



Because MoO₃ can form eutectic liquid solution with Li₂O at >525 °C,^[43] the surficial leaching can be uniformly done by wetting the whole particle with the molten molybdate. The high temperature can anneal the leftover crystal, eliminating Li/O vacancies to get a dense spinel shell with surface densification (Equation (3))



Liquid-phase diffusion is far more rapid than solid-state diffusion, so Equation (2) must be rate-controlled by solid-state diffusion. If we use a small amount of MoO₃ (such as 4–5 wt%), and assuming that the MoO₃–Li₂O liquid forms a percolating network among the particles, the eutectic solution will only leach a small amount of Li₂O from the surface region before it reaches the saturated Li₂MoO₄. That means, depending on the amount of leaching aid (MoO₃) and the leaching temperature and time, it is

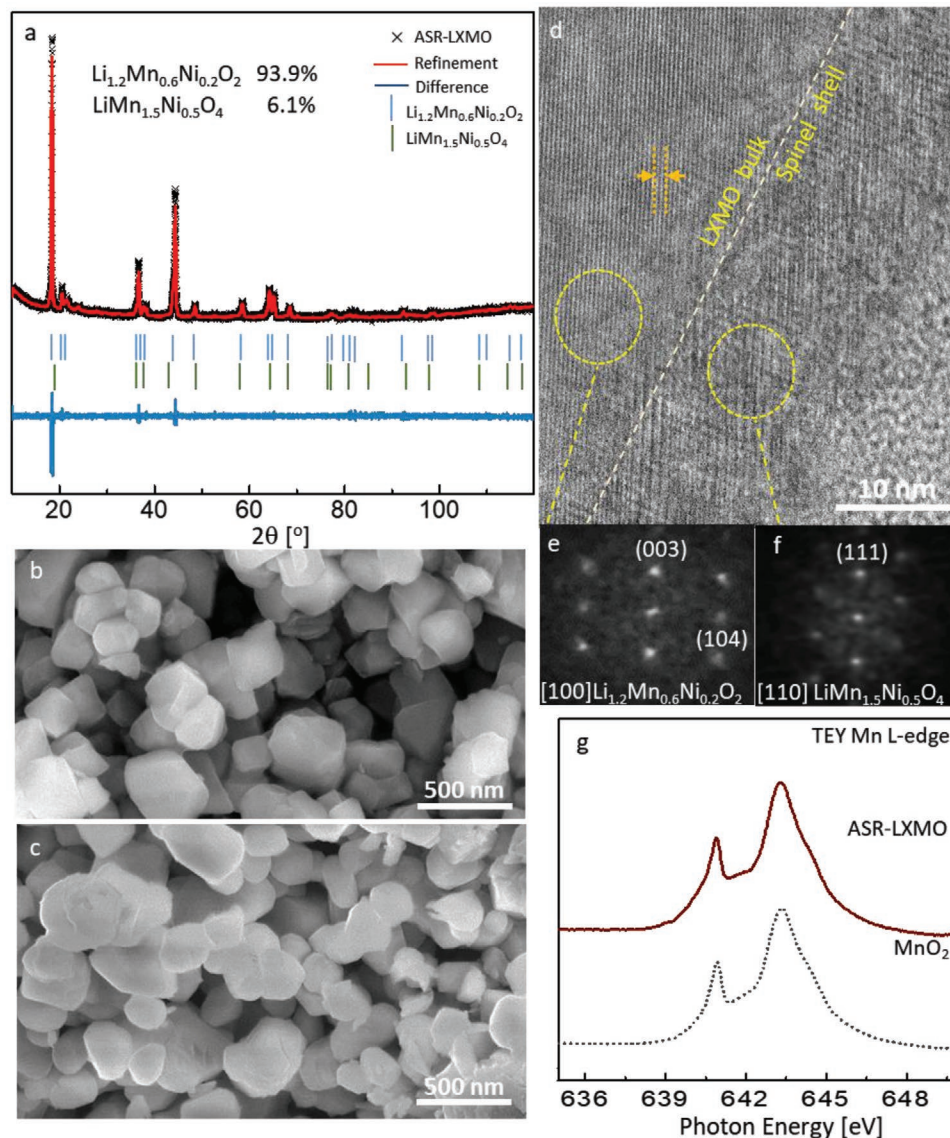


Figure 2. Characterization of the ASR-LXMO particles. a) The X-ray diffraction pattern of the ASR-LXMO particles, with the Rietveld refinement with $\text{Li}_{1.2}\text{Mn}_{0.6}\text{Ni}_{0.2}\text{O}_2$ and $\text{LiMn}_{1.5}\text{Ni}_{0.5}\text{O}_4$ phases. The SEM images of P-LXMO b) and ASR-LXMO c) particles. d) The HRTEM image of the ASR-LXMO particle after FIB preparation, indicating that the particle has a core with layered structure and a shell with spinel-like phase, which uniformly surrounds and encloses the LXMO core. FFT patterns transformed from the spinel surface e) and LXMO bulk f), as marked in (d) with yellow circles. g) sXAS TEY Mn L_3 -edge of the ASR-LXMO particles, showing that it agrees well with that of the standard MnO_2 reference.

controllable to conduct ASR only at the particle surface without infecting the LXMO bulk. Since molten MoO_3 only leaches Li_2O but does not dissolve Mn or Ni,^[42] this molten-molybdate leaching is a “scarless” treatment and can be used to leach quantitative amount of Li_2O from the particle to create a desirable ASR profile. This leaching process is quite scalable, and the side product Li_2MoO_4 on the particle surface can be simply removed with water washing, as Li_2MoO_4 is very water-soluble.

We performed diverse characterizations to confirm the establishment of ASR-LXMO. The XRD patterns in Figure S1 (Supporting Information) showed that after the leaching by molten molybdate, Li_2MoO_4 was generated in the product, which verified that Li_2O was leached from P-LXMO, then it was totally removed after water washing. The ICP analysis in Table S1 (Supporting Information) verified that the Li component in the particle

decreased after ASR, while Mn and Ni remained unchanged. In Figure 2a, the XRD pattern after ASR indicated the generation of $\text{LiMn}_{1.5}\text{Ni}_{0.5}\text{O}_4$ spinel in ASR-LXMO, which can be quantified as 6.1 wt% with Rietveld refinement (Table S2, Supporting Information). By comparing the SEM images before and after ASR in Figure 2b,c, the particles became more spherical in shape, which also indicated a cation rearrangement at the particle surface in ASR. The HRTEM images in Figure 2d and Figure S2 (Supporting Information) with FFT patterns in Figure 2e,f further demonstrated that a spinel shell has been created at the surface of ASR-LXMO particle, surrounding the LXMO core, which was only about 10 nm thick, but appeared to have completely and uniformly enclosed the LXMO bulk. Although NSR and ASR both transformed the layered LXMO lattice to spinel (or spinel-like) irreversibly, ASR that was conducted at 750 °C can anneal

most of oxygen vacancies $[V\ddot{o}]$,^[32,44] making $[V\ddot{o}]$ less than 0.001% in the crystal,^[32,33] while that produced in NSR was always higher than 1%.^[45] The soft X-ray absorption (sXAS) analysis in Figure 2g indicates that the Mn valence at the particle surface was still +4.0 after ASR, which corroborates that the amount of $[V\ddot{o}]$ in the shell was negligible after ASR, otherwise there must be Mn^{3+} ions if the spinel shell contains appreciable amount of $[V\ddot{o}]$.^[46,47] The ASR at high temperature also annealed out most of the prolific grain boundaries and/or exposed surfaces that could be generated in foreign coatings,^[48–50] which are preferential locations for GOM and stress-corrosion cracking (SCC) in electrolyte, making the spinel shell crystal robust to sufficiently prevent GOM and stabilize the cycling performance.

2.2. Stabilized Electrochemical Cycling in Half-Cells and Full-Cells

We prepared the cathode electrodes with 88% LXMO, 6% super P conductor and 6% PVDF binder, and coated on an Al foil (Experimental Section). The P-LXMO and ASR-LXMO cathodes were first tested in coin half-cells between 2.0 and 4.8 V. Figure 3a,b shows the voltage profiles of P-LXMO and

ASR-LXMO in different cycles: in the initial cycle, P-LXMO was charged to 327.4 mAh g⁻¹ and discharged to 235.2 mAh g⁻¹ under 60 mA g⁻¹; however, the voltage profile severely deformed after 200 cycles with obvious capacity decay. Though ASR-LXMO was only charged to 255.7 mAh g⁻¹ and discharged to 231.1 mAh g⁻¹ in the first cycle, it gradually increased to 252.9 mAh g⁻¹ after tens of cycles, and maintained a good voltage profile even after 200 cycles with less capacity and voltage decay. The cyclic capacity and average discharge voltage are shown in Figure 3c. It is clear that, both the capacity and voltage cycling of ASR-LXMO were significantly stabilized compared to P-LXMO, as the former had 237.4 mAh g⁻¹, with average discharge voltage 3.30 V while the later only retained 218.8 mAh g⁻¹ with 2.95 V after 200 cycles. The rates cycling performance can be found in Figure S3 (Supporting Information).

In half-cells, the Coulombic efficiency (CE) can be used to study the irreversible reactions, including capacity loss and side reactions in each cycle. Here, we used the Coulombic inefficiencies cumulant (CIC_n $\equiv \sum_{i=1}^n (CI)_i$, where $CI \equiv 100\% - CE$ and n is the cycle number)^[51,52] to compare the total irreversible capacities during the two cells cycling. As indicated in Figure 3c, the CIC of P-LXMO in the initial 30 cycles reached 48.00% while that of

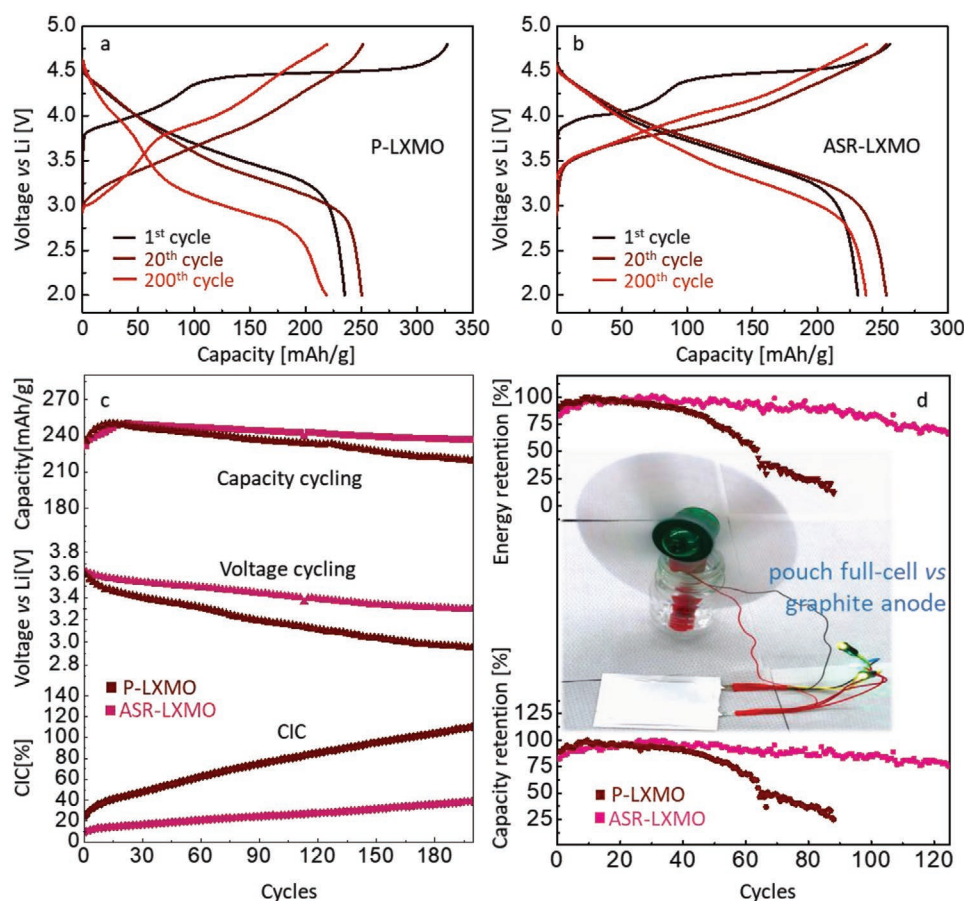


Figure 3. The electrochemical performances of P-LXMO and ASR-LXMO cathodes in coin half-cells and pouch full-cells. a,b) The charge/discharge profiles of P-LXMO a) and ASR-LXMO b) cathodes within 2.0–4.8 V in coin half-cells under a constant current of 60 mA g⁻¹. c) The cycling performance of discharge capacity, voltage, and Coulombic inefficiencies cumulant (CIC) of P-LXMO and ASR-LXMO cathodes within 2.0–4.8 V under 60 mA g⁻¹ in coin half-cells. d) The cycling retention of discharge capacity and energy density of P-LXMO and ASR-LXMO cathodes in pouch full-cells with commercial graphite anodes and lean-electrolyte (2 g A⁻¹ h⁻¹) within 2.8–4.65 V under 100 mA g⁻¹.

ASR-LXMO was only 16.58%; and after 200 cycles, the CIC of P-LXMO increased to 110.42% while that of ASR-LXMO was only 39.19%. As some side reactions, such as carbonate–electrolyte decomposition and radical shuttling in charging, also contributed to CIC, the lower CIC of ASR-LXMO suggested greatly suppressed side reactions with the electrolyte. We show that a significantly suppressed CO₂ release, suggesting an efficient prevention of the carbonate–electrolyte decomposition, was observed while charging ASR-LXMO in the later sections of this article.

As either Li source or electrolyte is abundant in coin half-cells, such CIC did not influence too much on the half-cell cycling within hundreds of cycles. However, while the undesirable side reactions consume electrolyte and Li ions, high CIC would deplete the electrolyte and Li quickly in a practical full-cell that is assembled with a graphite anode (free of Li source) and lean electrolyte. Therefore, the suppressed CIC in ASR-LXMO would especially stabilize the full-cell cycling. The cycling performances of ASR-LXMO and P-LXMO in pouch full-cells, matched with commercial graphite anodes and lean electrolyte (2 g A⁻¹ h⁻¹) were shown in Figure 3d. It indicated that while the P-LXMO full-cell cycling cannot survive 90 cycles, the ASR-LXMO full-cell retained 76% of discharge capacity and 66% of discharge energy density after 125 cycles. Notably, the energy density of the full-cell can reach 280 Wh kg⁻¹, higher than either LiCoO₂ or Ni-rich batteries (Discussion S1, Supporting Information). Though the ASR-LXMO full cycling stability is still far from the level necessary for commercialization, our results indicated that the prevented GOM has greatly stabilized the LXMO full-cell cycling, and it can be expected that the cycling can be further stabilized with a better electrolyte.

2.3. Prevented GOM and Stabilized HACR and Phase during Cycling

The stabilized cycling of ASR-LXMO mainly comes from the prevention of GOM. We first carried out the differential

electrochemical mass spectroscopy (DEMS) to monitor the O₂ and CO₂ evolution during the first charging of P-LXMO and ASR-LXMO. As Figure 4a showed, O₂ gas evolved profusely from P-LXMO between 4.5 and 4.7 V, which directly verified the oxygen escape (GOM). Meanwhile, CO₂ gas was also observed when charging P-LXMO, confirming that GOM from the cathode seriously oxidized the carbonate–electrolyte.^[13–15] As the electrolyte used in the practical cells are always very lean,^[22,23] the depletion of electrolyte can be the foremost life-limiting factor, as shown in Figure 3d. In contrast, little O₂ was observed when charging ASR-LXMO until 4.8 V, and there was also little CO₂ gas evolution. The DEMS result demonstrated that GOM has been efficiently stopped within the ASR-LXMO particle, which simultaneously prevented the electrolyte decomposition in cycling and promoted a much-extended full-cell cycling life with lean electrolyte, as shown in Figure 3d.

We also used sXAS at the In situ and Operando Soft X-ray Spectroscopy (IOS) beamline at NSLS-II of Brookhaven National Laboratory to track the oxidation states of oxygen ions in the cathode particles. As the detection depth of TEY sXAS can be up to a few nanometers in Li transition-metal oxides,^[53] the TEY sXAS can mainly collect the information from the particle surface. As shown in Figure 4b, the TEY sXAS O K-edge of P-LXMO and ASR-LXMO were similar in shape before charging, both close to that of MnO₂.^[54,55] After charging, the TEY O K-edge of P-LXMO changed obviously as the peak at ≈530 eV grew broad to cover the shoulder peak at ≈532 eV, while that of ASR-LXMO changed little, indicating different oxidation states of oxygen ions at the charged P-LXMO and ASR-LXMO particle surface.^[54,55] Through a quantitative analysis of the O K-edge intensity integral (Note S1, Supporting Information) which reflects the occupation of t_{2g} and e_g M–O hybridization orbitals,^[5,3,4,56] we can get that 318 mAh g⁻¹ was charged from the P-LXMO particle surface when charged to 4.8 V: since the cation redox (Ni^{2+/4+}) can maximally contribute 126 mAh g⁻¹ theoretically (0.2 × 2e per Li_{1.2}Mn_{0.6}Ni_{0.2}O₂), the oxygen anion redox had at least contributed 192 mAh g⁻¹ at the P-LXMO surface. In

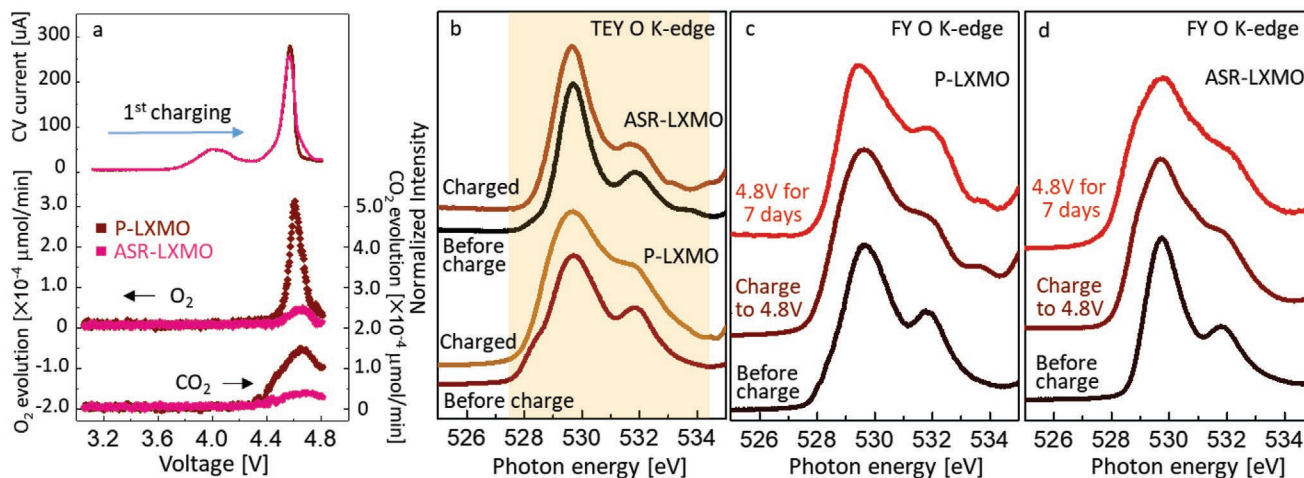


Figure 4. Tracking of GOM with DEMS and sXAS analysis in the P-LXMO and ASR-LXMO particles while charging. a) The DEMS in the 1st positive CV scanning of P-LXMO and ASR-LXMO cathodes to 4.8 V under 0.05 mV s⁻¹. The mass intensity at $m/z = 32$ was collected for O₂ and that at $m/z = 44$ was collected for CO₂. b) sXAS TEY O K-edge spectra of P-LXMO and ASR-LXMO before charge and after fully charged. c,d) sXAS PFY O K-edge spectra of P-LXMO c) and ASR-LXMO d) at different states of charge.

contrast, only 141 mAh g^{-1} was charged from the spinel shell at the ASR-LXMO particle surface according to the quantitative analysis of O K-edge (Note S1, Supporting Information) when charged to 4.8 V: since the cation redox in the spinel shell can theoretically afford 146.7 mAh g^{-1} , it does not entail significant oxidation of oxygen ions. The highly oxidized oxygen ions right at the P-LXMO surface would become mobile (the migration energy barrier of O^{2-} is above 2.4 eV, whereas that of the oxidized $\text{O}^{\alpha-}$ species can decrease to 0.9 eV^[7]) and easily escape from the particle at high voltage. In contrast, the oxygen ions can remain stable in the cation-redox-only spinel shell at the ASR-LXMO particle surface and efficiently shut down GOM within the whole particle in cycling.

We then investigated the oxidation states of oxygen ions in the particle bulk at high voltage, by tracking the partial fluorescence yield (PFY) sXAS O K-edges, which has a detection depth of more than 100 nm into the particle.^[53] As shown in Figure 4c,d, the oxygen ions in both P-LXMO and ASR-LXMO bulks were highly oxidized when charged to 4.8 V, as both the PFY O K-edges at 530 eV grew broad in the two materials after charging. However, when holding the two cathodes at 4.8 V for

7 days, the PFY O K-edge of P-LXMO obviously deformed in shape with the peak narrowing at 530 eV and peak reappearance at 532 eV, suggesting a reduction of electrode by “self-discharge” due to the GOM-resulted oxygen escape (as discussed before, when oxygen ion exits the particle, it has to leave behind its electrons). In contrast, the PFY O K-edge of ASR-LXMO remained very stable at the highly oxidized state, indicating a well-held charge on the bulk oxygen ions. The deeply penetrating spectroscopic signature of $\text{O}^{\alpha-}$ ($\alpha < 2$) over 7 days firmly validates the “solid oxygen” concept^[38,42] for cathode. The prevented GOM in ASR-LXMO agreed well with the DEMS analysis above, and which significantly stabilized the ASR-LXMO cycling performance as shown in Figure 3.

The prevented GOM in ASR-LXMO can stabilize the HACR voltage and capacity in cycling, while that were deranged in P-LXMO by GOM. As O K-edge reflects the overall capacity charged from the whole HACR,^[5,3,4,56] while M L-edge only refers to the M valence,^[3,57,58] we can coanalyze PFY sXAS O K-edges and inverse PFY (iPFY) sXAS M L-edges to distinguish the capacity contributions from O anion redox and M cation redox in cycling. Figure 5a–d shows the PFY sXAS O K-edges

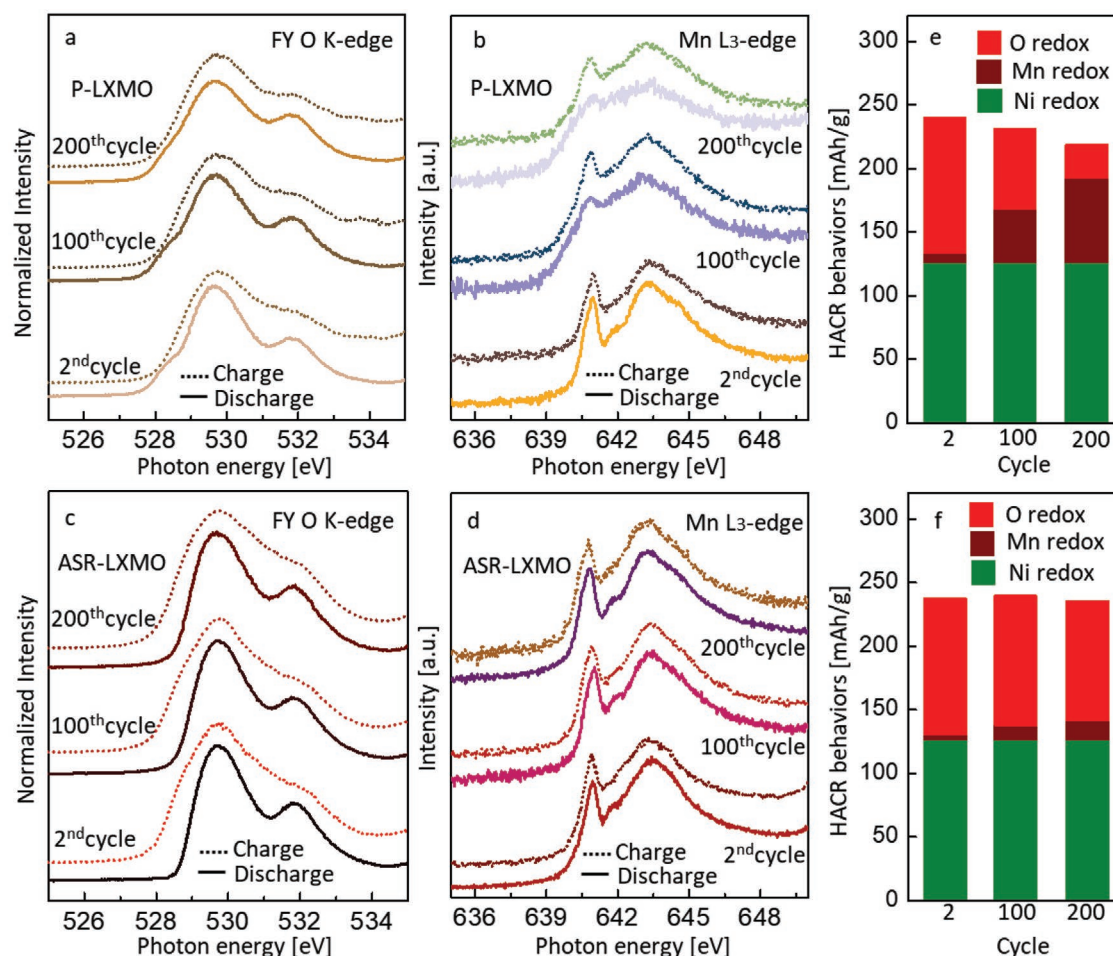


Figure 5. The hybrid O anion-redox and M cation-redox (HACR) behaviors in P-LXMO and ASR-LXMO in cycling. sXAS PFY O K-edge a) and iPFY Mn L₃ edge b) spectra of P-LXMO at discharge and full-charge states in different cycles. sXAS PFY O K-edge c) and iPFY Mn L₃ edge d) spectra of ASR-LXMO at discharge and full-charge states in different cycles. The capacity contributions from O, Mn, and Ni redox when fully charging P-LXMO e) and ASR-LXMO f) in different cycles.

and IPFY sXAS M L-edges of the two materials at discharged and charged states in different cycles. First, it can be seen that both the discharged Mn valences in the two materials were about +4 in the 2nd cycle. However, the average valence of Mn ions at discharged states in P-LXMO decreased to +3.80 and +3.65 after 100 and 200 cycles, while those in ASR-LXMO remained at +3.94 and +3.92 (Figure S4 and Table S3, Supporting Information). The reduced Mn valence in P-LXMO independently verified the disastrous continual GOM in P-LXMO cycling, but which was significantly suppressed in ASR-LXMO. With a quantitative analysis on O K-edges,^[3,57–59] we can get the total capacity charged from HACR (Table S4, Supporting Information), and with that on M L-edges, we can get the capacity from the M cation redox (Table S3 and Figure S5, Supporting Information) only, then we can get the capacity from O anion redox by the subtraction of the above two values. The capacity contributions from O anion redox and M cation redox of the two materials in different cycles were shown in Figure 5e,f. In the 2nd cycle, 240.1 and 238.2 mAh g⁻¹ were charged from P-LXMO and ASR-LXMO, respectively, which were quite similar. If we assume that both Ni and Mn ions can be charged to +4 before O anion redox was activated in charging, then Mn contributed 76 mAh g⁻¹ in P-LXMO, and 3.8 mAh g⁻¹ in ASR-LXMO in the 2nd cycle, and Ni ions in both cases contributed 126.1 mAh g⁻¹ (Figure S5, Supporting Information). Therefore, the remaining 106.4 mAh g⁻¹ from P-LXMO and 108.3 mAh g⁻¹ from ASR-LXMO must be charged from O anion redox. However, after prolonged cycling, the HACR behavior changed significantly between P-LXMO and ASR-LXMO. Though there were still 232.3 mAh g⁻¹ chargeable from P-LXMO in the 100th cycle, only 64.6 mAh g⁻¹ came from O anion redox, while the majority came from M cation redox (including 126.1 mAh g⁻¹ from Ni^{2+/4+} redox and 41.6 mAh g⁻¹ from Mn^{3+/4+} redox). After 200 cycles, the capacity from O anion redox decreased even further to 27.0 mAh g⁻¹ in P-LXMO, while that from Mn^{3+/4+} cation redox increased to 66.2 mAh g⁻¹. Because of $\Psi(\text{Mn}^{3+/4+}) < \Psi(\text{O}^{2-/4-})$, the increasing Mn^{3+/4+} cation-redox capacity, at the expense of O anion redox, thermodynamically decreased the working voltage of P-LXMO in cycling. In contrast, the HACR behavior of ASR-LXMO did not change much after 200 cycles, as only 15.1 mAh g⁻¹ from oxygen anion redox was replaced by Mn^{3+/4+} cation redox in the 200th cycle. Therefore, the prevented GOM in ASR-LXMO stabilized the HACR capacities and open-circuit voltages (thermodynamic voltage) in cycling.

The stabilized thermodynamic cycling voltage of ASR-LXMO can be demonstrated independently by the galvanostatic intermittent titration technique (GITT), by comparing the equilibrium voltage profiles (solid line) in the 200th cycle as shown in Figure 6a. After 200 cycles, the equilibrium voltage profile of ASR-LXMO maintained well, while that of P-LXMO seriously deformed. The efficiently suppressed cyclic voltage fading of ASR-LXMO agreed well with the stabilized HACR in the ASR-LXMO cycling (Figure 5f). Moreover, from Figure 6a we can see that the titration-voltage drop of ASR-LXMO (ΔE_t , excluding the Ohmic resistance) was also significantly suppressed compared to that of P-LXMO in the 200th cycle, which suggested that the kinetics of ASR-LXMO was stabilized in cycling as well. The Li⁺ diffusivities (D_{Li^+}) in P-LXMO and ASR-LXMO were calculated from GITT, and compared in Figure 6b. It is clear that the

average D_{Li^+} in ASR-LXMO was almost one order of magnitude higher than that in P-LXMO in the 200th cycle.

The well-maintained D_{Li^+} in ASR-LXMO can be attributed to the stabilized crystalline phase (prevented IPT) in cycling. Figure 6c–f shows the HRTEM images of P-LXMO and ASR-LXMO particles after 200 cycles. The P-LXMO particles after cycling, as same as that was widely reported,^[11,12] had a high amount of oxygen voids with rampant structural collapse and phase transformations everywhere (Figure 6c,d). However, the ASR-LXMO particle remained a dense crystal with little oxygen voids, and the bulk maintained a good layered structure (Figure 6e) all the way up to the artificially created shell (Figure 6f). The stabilized phase during the ASR-LXMO cycling significantly maintained the high D_{Li^+} and electrochemical kinetics in cycling.

Mn³⁺ dissolution from the cathode and deposition at the graphite anode is also a critical issue to prevent the application of Mn-rich LXMO cathode in full-cells, as it could block the Li⁺ transport through the solid electrolyte interface (SEI) at the graphite anode and kill the practical cell.^[18,20,21,40] As discussed above, most of the Mn ions were still in the +4 valence state during the ASR-LXMO cycling, while a massive amount of Mn⁴⁺ ions were reduced to Mn³⁺ in the P-LXMO cycling, so the Mn³⁺ dissolution can be significantly prevented from ASR-LXMO cathode, as Mn⁴⁺ has little dissolution in the carbonate electrolyte.^[28] We used EDS mapping and ICP to measure the Mn deposition at the graphite anodes that were disassembled from the full-cells after 120 cycles. As shown in Figure S6 and Figure S7 (Supporting Information), while the signals of C and F were similar on the two graphite anodes from P-LXMO and ASR-LXMO cells, there was obvious Mn deposition on the graphite anode from the P-LXMO cell, but much less Mn on that from the ASR-LXMO cell. The ICP analysis on the graphite anodes in Table S5 (Supporting Information) further verified that the amount of deposited Mn at the graphite anode from the ASR-LXMO cell was only about 1/4 that from the P-LXMO cell after 125 cycles. The suppressed Mn dissolution from ASR-LXMO cathode and deposition at anode greatly helped improve the cycling life of the pouch full-cell, as shown in Figure 3d.

3. Conclusions

In Li-rich oxides (LXMO) cathode particles, the heavy participation of oxygen anion redox results in global oxygen migration (GOM) and natural surface reconstruction (NSR). NSR would grow throughout the whole particle in the prolonged cycles, which not only causes Mn⁴⁺ reduction, shifting HACR capacities and thermodynamic voltages by introducing more Mn^{3+/4+} cation redox in place of O^{2-/4-} anion redox, but also increases the kinetic impedance. We conducted an artificial surface prereconstruction (ASR), with a molten molybdate leaching at 750 °C to create a crystal dense spinel shell, to prevent GOM in cycling. DEMS and sXAS demonstrated that GOM was efficiently prevented while charging, so that both the HACR thermodynamic voltages and kinetic impedance were significantly stabilized after hundreds of cycles. Additionally, the prevented GOM in ASR-LXMO also stopped the carbonate-electrolyte decomposition and Mn dissolution in cycling, so

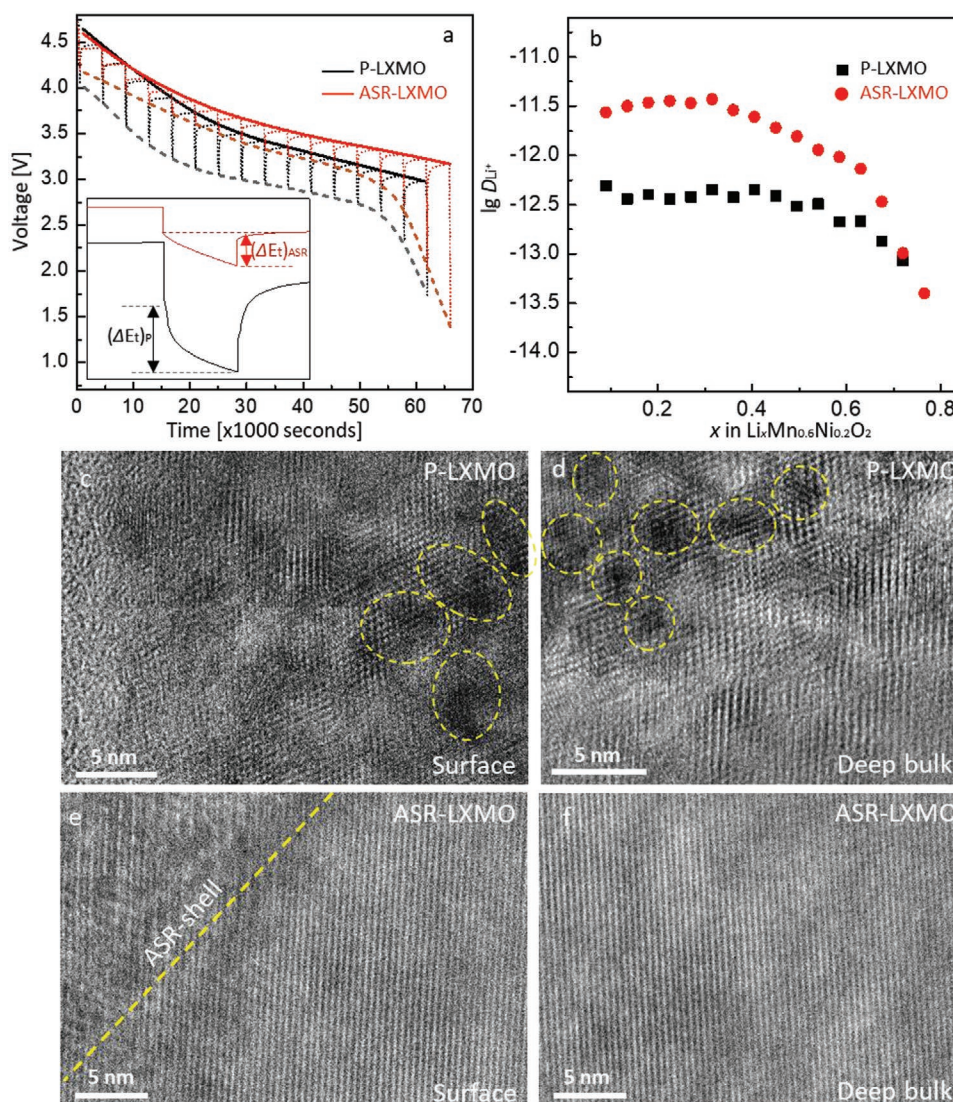


Figure 6. The electrochemical kinetics and phases of P-LXMO and ASR-LXMO cathodes after 200 cycles. a) GITT curve in discharging of P-LXMO and ASR-LXMO in the 200th cycle. b) The Li^+ diffusivity in P-LXMO and ASR-LXMO at different states of discharge in the 200th cycle, calculated from (a). The HRTEM images of the P-LXMO particles after FIB preparation, picked from the particle surface c) and particle bulk d). The yellow circle marks the oxygen voids with phase collapse in the particle. The HRTEM images of the ASR-LXMO particles after FIB preparation, picked from the particle surface e) and particle bulk f).

that ASR-LXMO can survive a much-extended cycling life in a pouch full-cell.

This molten MoO_3 leaching can also be conducted on many other cathode materials. As is well known, most layered cathode (LMO) materials, such as LCO and Ni-rich NMC cathodes also suffer from oxygen release and cycling decay when cycled to higher voltages (above 4.5 V). If we perform this molten-oxide leaching surface treatment on these cathode materials to leach some Li from the particle surface ahead of cycling, establishing a “Li-poor” shell to completely enclose the LMO lattice, then the oxygen migration can be stopped within the particle to stabilize high voltage cycling. Moreover, we can also look for other leaching agents that can leach elements other than Li from the cathode particle. Because the Ni at the Ni-rich particle surface is quite catalytically active and always causes side reactions with

the electrolyte, we may use some specific leaching agent to extract some Ni out from the particle surface, creating an integral Ni-poor and O-poor passivation shell to fully cover and protect the Ni-rich lattice and improve the cycling stability.

4. Experimental Section

Synthesis of the Pristine Li-Rich Particles: The Li-rich $\text{Li}_{1.20}\text{Mn}_{0.6}\text{Ni}_{0.2}\text{O}_2$ particles were prepared by a wet coprecipitation method followed by a solid-state reaction process. First, $\text{MnSO}_4 \cdot \text{H}_2\text{O}$ (Reagent Plus, $\geq 99\%$, Sigma-Aldrich), $\text{NiSO}_4 \cdot 6\text{H}_2\text{O}$ (ACS Reagent, $\geq 98\%$, Sigma-Aldrich) were completely dissolved in deionized water with a molar ratio of 3:1. Then the solution was titrated into 0.5 mol/L NaOH solution (with ammonia water added as buffering solution), with stirring in 60 °C water bath. Stirring was kept for 2 h at 60 °C and the solution was

cooled to room temperature in air. The sediments were separated from water by centrifugation and washed with water. This process was repeated 3 times. Subsequently the product was dried at 110 °C in a vacuum oven to get a powder precursor. After that, the precursor was mixed with LiOH·H₂O (ACS Reagent, ≥98%, Sigma-Aldrich) and heated at 900 °C for 12 h to get the pristine Li-rich Li_{1.20}Mn_{0.6}Ni_{0.2}O₂ material (P-LXMO).

Artificial Surface Prereconstruction on P-LXMO: 4–5 wt% of (NH₄)₆Mo₇O₂₄·4H₂O was dissolved in deionized water and the pH was adjusted to 9–10 with NH₃·H₂O, then the as-prepared P-LXMO material was put into the solution and was dispersed with high power ultrasound for 30 min, and then evaporated with stirring in 90 °C water bath. Then, the powder was milled and pressed and then it was heated at 300 °C for 2 h and 750 °C for 8 h. Then the product was milled again and dispersed in deionized water by ultrasound and the solid is separated by centrifugation. At last, the solid was dried at 200 °C in a vacuum oven for 3 h to get the final product (ASR-LXMO).

Characterizations: X-ray diffraction was performed on a PANalytical X'Pert PRO X-ray diffractor using Cu target under 45 kV, 40 mA. The data was collected with 2° min⁻¹ and analyzed with the HighScore Plus software. Scanning electron microscopy was performed on a Zeiss Merlin high-resolution scanning electron microscope. The sample for atomic resolution STEM imaging was prepared by focused ion beam (FIB) lift-out using the FEI Helios 600 with Ga ion source. A platinum layer is deposited on top of a particle to protect the cathode particle before the lift-out. The 2K images (2048 × 2048 pixels) are acquired with a dwell time of 16 μs per pixel. High-resolution transmission electron microscopy (HRTEM) images were taken on a JEOL 2010F at 200 kV.

Soft X-ray absorption spectroscopy measurements were carried out at the IOS (23-ID-2) beamline at the National Synchrotron Light Source II (NSLS-II) at Brookhaven National Laboratory. Spectra were acquired in total electron yield (TEY), PFY and IPFY modes. The estimated incident X-ray energy resolution was ≈0.05 eV at the O K-edge. The monochromator absorption features and beam instabilities were normalized out by dividing the detected TEY, PFY and IPFY signals by the drain current of a clean gold I0 mesh placed in the incident beam. TEY spectra were recorded from the drain current of the sample and PFY/IPFY data were acquired using a Vortex EM silicon drift detector. iPFY spectra for the metal L-edges were obtained by monitoring the non-resonant fluorescence of oxygen while scanning the incident X-ray at the metal L-edge energy. The sXAS spectra for O K-edge were recorded over a wide energy range from 520 to 565 eV covering energies well below and above sample absorptions. The normalization of the O K-edge was performed according to the following procedure^[5]: 1) I₀ normalization: the sample signal is divided by the incident intensity measured from the sample drain current from a freshly coated Au mesh inserted into the beam path before the X-rays can impinge on the sample. 2) A linear, sloping background is removed by fitting a line to the flat low energy region (520–524 eV) of the sXAS spectrum. 3) The spectrum is normalized by setting the flat low energy region to zero and the postedge to unity (unit edge jump). The photon energy selected for the post edge was 560 eV, beyond the region of any absorption (peaks).

Electrochemical Test: Both CR2032 coin cells and pouch cells were used for the electrochemical tests in this work. The cathode was comprised of 88wt% active material, 6wt% carbon black, and 6wt% polyvinylidene fluoride (PVDF) binder, which was pasted on an Al current collector. Half-cells were fabricated with an anode of Li metal sheets; a separator of Celgard 2400 polymer; and a commercial electrolyte solution of 1.2 M LiPF₆ dissolved in a mixture of EC and DEC with a volume ratio of 1:1. Pouch full-cells were fabricated with the above cathodes, commercial graphite anode (double-side coated), a separator of Celgard 2400 polymer and a commercial high voltage electrolyte solution (ordered from Soulbrain <http://soulbrainmi.com/technology/>) of 1.2 M LiPF₆ dissolved in a mixture of EC and DEC, etc., with 2wt% vinylene carbonate additive. The loading density of cathode was about 13 mg cm⁻² with ≈3.5 mAh cm⁻² (tested in half-cell under 0.1 C); the commercial graphite anode had a loading density of ≈12 mg cm⁻² with

≈3.8 mAg cm⁻² (tested in half-cell under 0.1 C). The pouch full-cells were fabricated with double layers of electrodes (one graphite anode foil with double-sides coated and two cathode foils with single-side coated). The amount of electrolyte added was about 2 g A⁻¹ h⁻¹ in the pouch cell. A LAND CT2001A eight-channel automatic battery test system (Wuhan Lanhe Electronics) was used for charging/discharging of the cells. An electrochemical workstation (Gamry Instr., Reference 3000) was used for the cyclic voltammetry scan. Galvanostatic intermittent titration technique was also performed on electrochemical workstation with constant current for 200 s followed with 3600 s relaxation with upper voltage of 4.8 V and lower limitation of 2.0 V. The electrochemical tests were all carried out at room temperature. A self-made quantitative DEMS was used to detect and analyze the gas during the cell testing. Two glued polyether ether ketone (PEEK) capillary tubes were used as inlet and outlet of gas. The cell was fabricated in a glove box where O₂ < 0.1 ppm. Then, the output tube was connected to a commercial Thermo mass spectrometer (MS). High-purity Ar gas was used as the carrier gas with a flow rate of 3 mL min⁻¹ during the cycling process. In the cyclic voltammetry process, the scan rate was 0.05 mV s⁻¹, and MS spectra were collected every 30 seconds.

Supporting Information

Supporting Information is available from the Wiley Online Library or from the author.

Acknowledgements

The authors acknowledge the support by Wuxi Weifu High-Technology Group Co., Ltd. This research used resources of the Center for Functional Nanomaterials and the 23-ID-2 (IOS) beamline of the National Synchrotron Light Source II, which are U.S. Department of Energy (DOE) Office of Science User Facilities operated for the DOE Office of Science by Brookhaven National Laboratory under Contract No. DE-SC0012704. Also, this work was performed in part at the Center for Nanoscale Systems (CNS), a member of the National Nanotechnology Coordinated Infrastructure Network (NNCI) supported by the National Science Foundation under NSF Award No. 1541959.

Conflict of Interest

The authors declare no conflict of interest.

Author Contributions

Z.Z. and J.L. conceived and designed the experiments. Z.Z. synthesized the materials and performed the materials characterizations and electrochemical tests. R.G. performed the TEM imaging. I.W. and A.H. measured the soft X-ray absorption. Z.Z. and I.W. carried out the sXAS data analysis. Z.Z. and J.L. wrote the paper. All authors analyzed the data, discussed the results, and commented on the manuscript.

Keywords

cathode materials, Li ion batteries, surface reconstruction

Received: March 29, 2020

Revised: June 17, 2020

Published online:

- [1] D.-H. Seo, J. Lee, A. Urban, R. Malik, S. Kang, G. Ceder, *Nat. Chem.* **2016**, *8*, 692.
- [2] E. Y. Hu, X. Yu, R. Lin, X. Bi, J. Lu, S. Bak, K. W. Nam, H. L. Xin, C. Jaye, D. A. Fischer, K. Amine, X. Q. Yang, *Nat. Energy* **2018**, *3*, 690.
- [3] K. H. Dai, J. Wu, Z. Zhuo, Q. Li, S. Sallis, J. Mao, G. Ai, C. Sun, Z. Li, W. E. Gent, W. C. Chueh, Y.-D. Chuang, R. Zeng, Z. X. Shen, F. Pan, S. Yan, L. F. J. Piper, Z. Hussain, G. Liu, W. Yang, *Joule* **2019**, *3*, 518.
- [4] M. Oishi, K. Yamanaka, I. Watanabe, K. Shimoda, T. Matsunaga, H. Arai, Y. Ukyo, Y. Uchimoto, Z. Ogumi, T. Ohta, *J. Mater. Chem. A* **2016**, *4*, 9293.
- [5] K. Luo, M. R. Roberts, R. Hao, N. Guerrini, D. M. Pickup, Y.-S. Liu, K. Edström, J. Guo, A. V. Chadwick, L. C. Duda, P. G. Bruce, *Nat. Chem.* **2016**, *8*, 684.
- [6] M. Li, T. Liu, X. Bi, Z. Chen, K. Amine, C. Zhong, J. Lu, *Chem. Soc. Rev.* **2020**, *49*, 1688.
- [7] E. Lee, K. A. Persson, *Adv. Energy Mater.* **2014**, *4*, 1400498.
- [8] W. E. Gent, K. Lim, Y. Liang, Q. Li, T. Barnes, S. J. Ahn, K. H. Stone, M. Mcintire, J. Hong, J. H. Song, Y. Li, A. Mehta, S. Ermon, T. Tyliczszak, D. Kilcoyne, D. Vine, J. H. Park, S. K. Doo, M. F. Toney, W. Yang, D. Prendergast, W. C. Chueh, *Nat. Commun.* **2017**, *8*, 2091.
- [9] J. M. Zheng, S. Myeong, W. Cho, P. Yan, J. Xiao, C. Wang, J. Cho, J. G. Zhang, *Adv. Energy Mater.* **2017**, *7*, 1601284.
- [10] A. Manthiram, J. C. Knight, S. T. Myung, S. M. Oh, Y. K. Sun, *Adv. Energy Mater.* **2016**, *6*, 1501010.
- [11] A. Singer, M. Zhang, S. Hy, D. Cela, C. Fang, T. A. Wynn, B. Qiu, Y. Xia, Z. Liu, A. Ulvestad, N. Hua, J. Wingert, H. Liu, M. Sprung, A. V. Zozulya, E. Maxey, R. Harder, Y. S. Meng, O. G. Shpyrko, *Nat. Energy* **2018**, *3*, 641.
- [12] P. F. Yan, J. Zheng, Z. K. Tang, A. Devaraj, G. Chen, K. Amine, J.-G. Zhang, L.-M. Liu, C. Wang, *Nat. Nanotechnol.* **2019**, *14*, 602.
- [13] B. D. McCloskey, D. S. Bethune, R. M. Shelby, G. Girishkumar, A. C. Luntz, *J. Phys. Chem. Lett.* **2011**, *2*, 1161.
- [14] S. A. Freunberger, Y. Chen, Z. Peng, J. M. Griffin, L. J. Hardwick, F. Bardé, P. Novák, P. G. Bruce, *J. Am. Chem. Soc.* **2011**, *133*, 8040.
- [15] P. G. Bruce, S. A. Freunberger, L. J. Hardwick, J. M. Tarascon, *Nat. Mater.* **2012**, *11*, 19.
- [16] C. Wang, L. Xing, J. Vatamanu, Z. Chen, G. Lan, W. Li, K. Xu, *Nat. Commun.* **2019**, *10*, 3423.
- [17] S. Komaba, N. Kumagai, Y. Kataoka, *Electrochim. Acta* **2002**, *47*, 1229.
- [18] H. Tsunekawa, S. Tanimoto, A. R. Marubayashi, M. Fujita, K. Kifune, M. Sano, *J. Electrochem. Soc.* **2002**, *149*, A1326.
- [19] J. Lu, C. Zhan, T. Wu, J. Wen, Y. Lei, A. J. Kropf, H. Wu, D. J. Miller, J. W. Elam, Y. K. Sun, X. Qiu, K. Amine, *Nat. Commun.* **2014**, *5*, 5693.
- [20] I. H. Cho, S. S. Kim, S. C. Shin, N. S. Choi, *Electrochem Solid-State Lett.* **2010**, *13*, A168.
- [21] S. Komaba, T. Itabashi, T. Ohtsuka, H. Groult, N. Kumagai, B. Kaplan, H. Yashiro, *J. Electrochem. Soc.* **2005**, *152*, A937.
- [22] M. Hagen, D. Hanselmann, K. Ahlbrecht, R. Maça, D. Gerber, J. Tübke, *Adv. Energy Mater.* **2015**, *5*, 1401986.
- [23] S. Chen, C. Niu, H. Lee, Q. Li, L. Yu, W. Xu, J.-G. Zhang, E. J. Dufek, M. S. Whittingham, S. Meng, J. Xiao, J. Liu, *Joule* **2019**, *3*, 1094.
- [24] H. Xu, S. Li, C. Zhang, X. Chen, W. Liu, Y. Zheng, Y. Xie, Y. Huang, J. Li, *Energy Environ. Sci.* **2019**, *12*, 2991.
- [25] S. H. Guo, H. Yu, P. Liu, X. Liu, D. Li, M. Chen, M. Ishida, H. Zhou, *J. Mater. Chem. A* **2014**, *2*, 4422.
- [26] F. H. Zheng, C. Yang, X. Xiong, J. Xiong, R. Hu, Y. Chen, M. Liu, *Angew. Chem., Int. Ed.* **2015**, *54*, 13058.
- [27] M. Li, J. Lu, *Science* **2020**, *367*, 979.
- [28] L. Suo, W. Xue, M. Gobet, S. G. Greenbaum, C. Wang, Y. Chen, W. Yang, Y. Li, J. Li, *Proc. Natl. Acad. Sci. USA* **2018**, *115*, 1156.
- [29] D. Kim, G. Sandi, J. R. Croy, K. G. Gallagher, S.-H. Kang, E. Lee, M. D. Slater, C. S. Johnson, M. M. Thackeray, *J. Electrochem. Soc.* **2013**, *160*, A31.
- [30] B. R. Long, J. R. Croy, J. S. Park, J. Wen, D. J. Miller, M. M. Thackeray, *J. Electrochem. Soc.* **2014**, *161*, A2160.
- [31] E. S. Lee, A. Huq, A. Manthiram, *J. Power Sources* **2013**, *240*, 193.
- [32] T. Nakamura, H. Gao, K. Ohta, Y. Kimura, Y. Tamenori, K. Nitta, T. Ina, M. Oishi, K. Amezawa, *J. Mater. Chem. A* **2019**, *7*, 5009.
- [33] L. P. Wang, H. Li, X. J. Huang, E. Baudrin, *Solid State Ionics* **2011**, *193*, 32.
- [34] Z. Zhu, Z. D. Qilu, H. Y. Yu, *Electrochim. Acta* **2014**, *115*, 290.
- [35] Z. Zhu, H. Yan, D. Zhang, W. Li, Q. Lu, *J. Power Sources* **2013**, *224*, 13.
- [36] Z. Zhu, D. Zhang, H. Yan, W. Li, Qilu, *J. Mater. Chem. A* **2013**, *1*, 5492.
- [37] Z. Zhu, D. Yu, Z. Shi, R. Gao, X. Xiao, I. Waluyo, M. Ge, Y. Dong, W. Xue, G. Xu, W. K. Lee, A. Hunt, J. Li, *Energy Environ. Sci.* **2020**, *13*, 1865.
- [38] Z. Zhu, A. Kushima, Z. Yin, L. Qi, K. Amine, J. Lu, J. Li, *Nat. Energy* **2016**, *1*, 16111.
- [39] Y. Qiao, K. Z. Jiang, H. Deng, H. S. Zhou, *Nat. Catal.* **2019**, *2*, 1035.
- [40] C. Zhan, J. Lu, A. Jeremy Kropf, T. Wu, A. N. Jansen, Y. K. Sun, X. Qiu, K. Amine, *Nat. Commun.* **2013**, *4*, 2437.
- [41] H. Wang, E. Rus, T. Sakuraba, J. Kikuchi, Y. Kiya, H. D. Abruña, *Anal. Chem.* **2014**, *86*, 6197.
- [42] Z. Zhu, D. Yu, Y. Yang, C. Su, Y. Huang, Y. Dong, I. Waluyo, B. Wang, A. Hunt, X. Yao, J. Lee, W. Xue, J. Li, *Nat. Energy* **2019**, *4*, 1049.
- [43] M. Moser, D. Klimm, S. Ganschow, A. Kwasniewski, K. Jacobs, *Cryst. Res. Technol.* **2008**, *43*, 350.
- [44] K. Takahashi, M. Saitoh, M. Sano, M. Fujita, K. Kifune, *J. Electrochem. Soc.* **2004**, *151*, A173.
- [45] B. Qiu, M. Zhang, L. Wu, J. Wang, Y. Xia, D. Qian, H. Liu, S. Hy, Y. Chen, K. An, Y. Zhu, Z. Liu, Y. S. Meng, *Nat. Commun.* **2016**, *7*, 12108.
- [46] J. Song, D. W. Shin, Y. Lu, C. D. Amos, A. Manthiram, J. B. Goodenough, *Chem. Mater.* **2012**, *24*, 3101.
- [47] J. Xiao, X. Chen, P. V. Sushko, M. L. Sushko, L. Kovarik, J. Feng, Z. Deng, J. Zheng, G. L. Graff, Z. Nie, D. Choi, J. Liu, J.-G. Zhang, M. S. Whittingham, *Adv. Mater.* **2012**, *24*, 2109.
- [48] X. D. Zhang, J.-L. Shi, J. Y. Liang, Y.-X. Yin, J. N. Zhang, X.-Q. Yu, Y.-G. Guo, *Adv. Mater.* **2018**, *30*, 1801751.
- [49] G. Li, X. Feng, Y. Ding, S. Ye, X. Gao, *Electrochim. Acta* **2012**, *78*, 308.
- [50] K. Mu, Y. Cao, G. Hu, K. Du, H. Yang, Z. Gan, Z. Peng, *Electrochim. Acta* **2018**, *273*, 88.
- [51] Y. Jin, S. Li, A. Kushima, X. Zheng, Y. Sun, J. Xie, J. Sun, W. Xue, G. Zhou, J. Wu, F. Shi, R. Zhang, Z. Zhu, K. So, Y. Cui, J. Li, *Energy Environ. Sci.* **2017**, *10*, 580.
- [52] Y. H. Zheng, Y. Lu, X. Qi, Y. Wang, L. Mu, Y. Li, Q. Ma, J. Li, Y. S. Hu, *Energy Storage Mater.* **2019**, *18*, 269.
- [53] R. Qiao, L. A. Wray, J. H. Kim, N. P. W. Pieczonka, S. J. Harris, W. Yang, *J. Phys. Chem. C* **2015**, *119*, 27228.
- [54] K. Luo, M. R. Roberts, N. Guerrini, N. Tapia-Ruiz, R. Hao, F. Massel, D. M. Pickup, S. Ramos, Y.-S. Liu, J. Guo, A. V. Chadwick, L. C. Duda, P. G. Bruce, *J. Am. Chem. Soc.* **2016**, *138*, 11211.
- [55] K. Luo, M. R. Roberts, R. Hao, N. Guerrini, D. M. Pickup, Y.-S. Liu, K. Edström, J. Guo, A. V. Chadwick, L. C. Duda, P. G. Bruce, *Nat. Chem.* **2016**, *8*, 684.
- [56] K. Luo, M. R. Roberts, N. Guerrini, N. Tapia-Ruiz, R. Hao, F. Massel, D. M. Pickup, S. Ramos, Y.-S. Liu, J. Guo, A. V. Chadwick, L. C. Duda, P. G. Bruce, *J. Am. Chem. Soc.* **2016**, *138*, 11211.
- [57] R. M. Qiao, Y. Wang, P. Olalde-Velasco, H. Li, Y. S. Hu, W. Yang, *J. Power Sources* **2015**, *273*, 1120.
- [58] M. Risch, K. A. Stoerzinger, B. Han, T. Z. Regier, D. Peak, S. Y. Sayed, C. Wei, Z. Xu, Y. Shao-Horn, *J. Phys. Chem. C* **2017**, *121*, 17682.
- [59] Q. H. Li, R. Qiao, L. A. Wray, J. Chen, Z. Zhuo, Y. Chen, S. Yan, F. Pan, Z. Hussain, W. Yang, *J. Phys. D: Appl. Phys.* **2016**, *49*, 413003.

ADVANCED ENERGY MATERIALS

Supporting Information

for *Adv. Energy Mater.*, DOI: 10.1002/aenm.202001120

Stabilized Co-Free Li-Rich Oxide Cathode Particles with An
Artificial Surface Prereconstruction

*Zhi Zhu, Rui Gao, Iradwikanari Waluyo, Yanhao Dong,
Adrian Hunt, Jinhyuk Lee, and Ju Li**

Supplementary Information

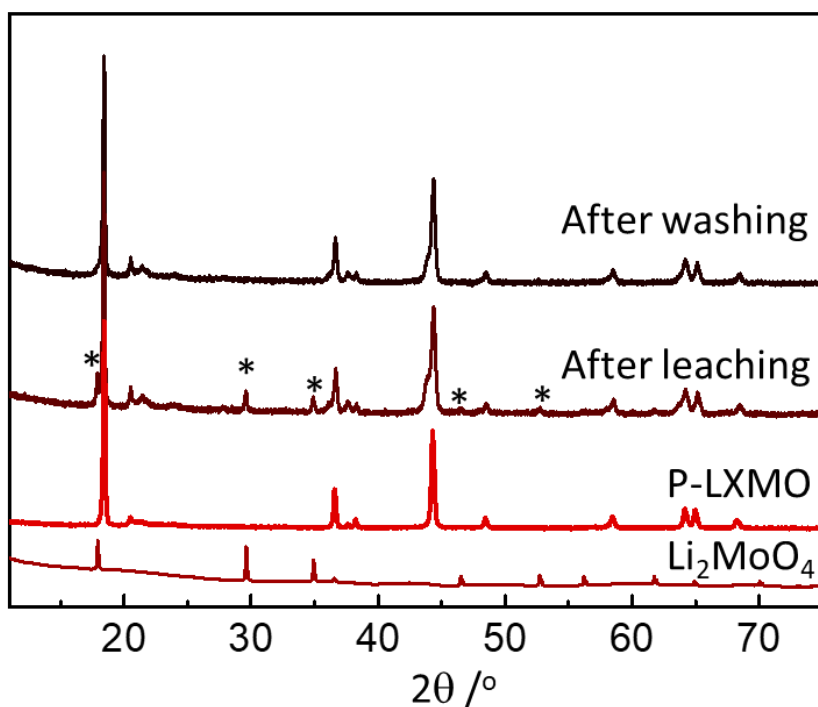
Stabilized Co-free Li-rich oxide cathode particles with an artificial surface pre-reconstruction

Zhi Zhu¹, Rui Gao¹, Iradwikanari Waluyo², Yanhao Dong¹, Adrian Hunt², Jinhyuk Lee¹ and Ju Li^{1*}

¹Department of Nuclear Science and Engineering and Department of Materials Science and Engineering, Massachusetts Institute of Technology, Cambridge, MA 02139, USA.

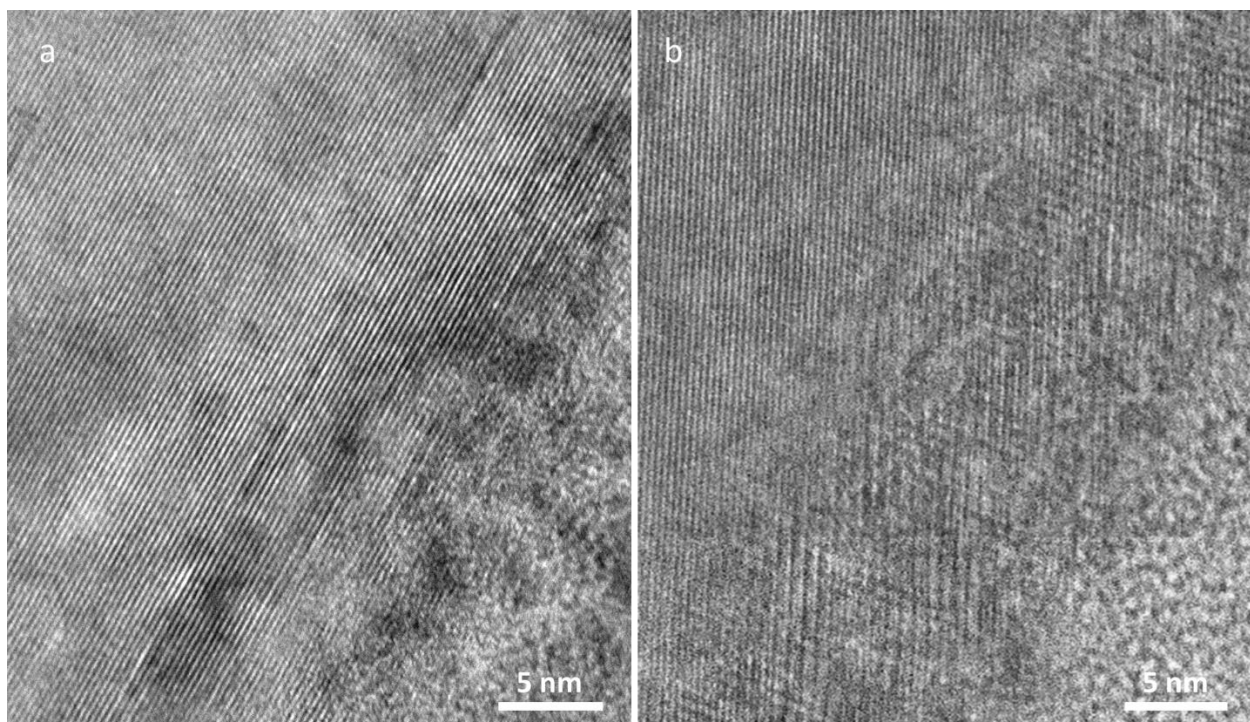
²National Synchrotron Light Source II, Brookhaven National Laboratory, Upton, NY 11973, USA

(*Corresponding author: Ju Li, Email: liju@mit.edu)

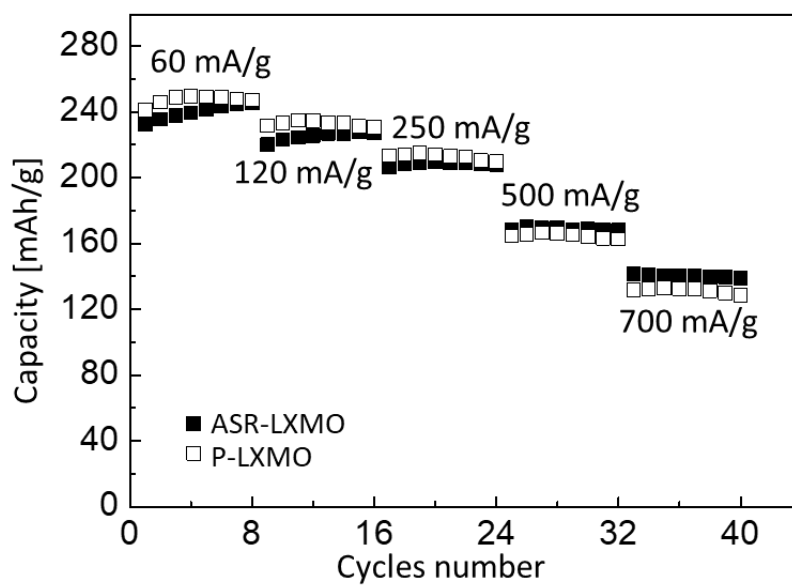


Supplementary Figure 1 XRD patterns of the intermediate product after MoO_3 leaching at ≥ 750 °C. The new peaks after MoO_3 leaching were totally matched with the one of pure Li_2MoO_4 with spinel $\text{Fd}3\text{m}$ crystal structure (sd_0307446).¹

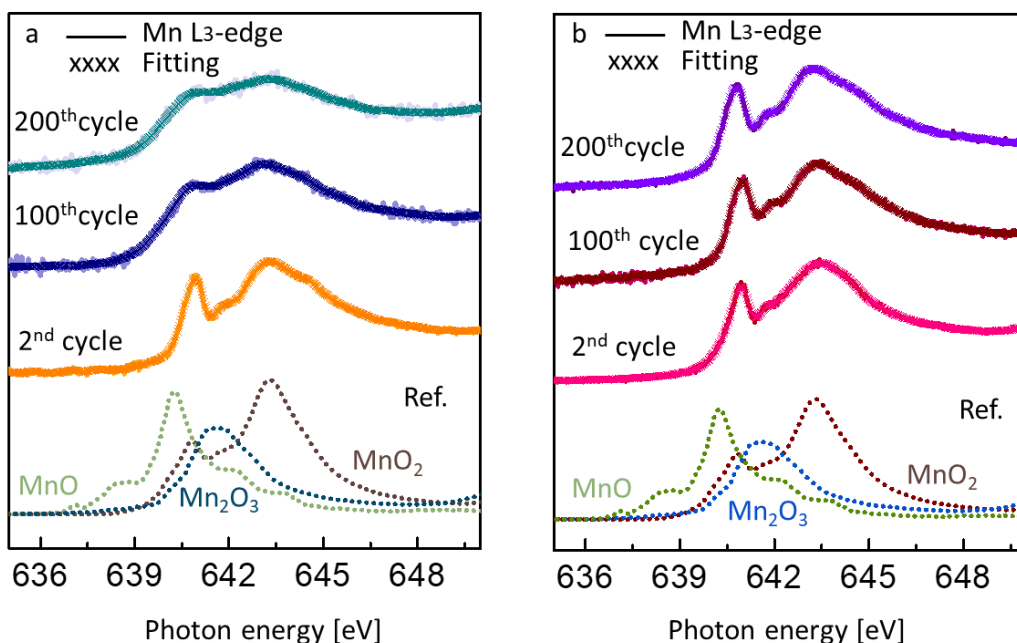
(https://materials.springer.com/isp/crystallographic/docs/sd_0307446)



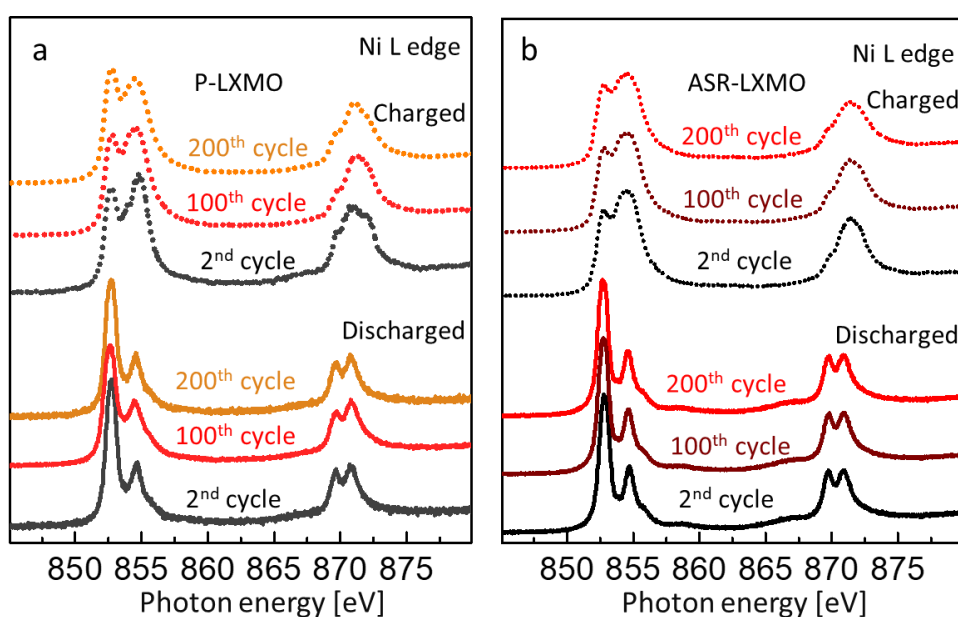
Supplementary Figure 2 HRTEM images of the (a) P-LXMO and (b) ASR-LXMO particles near the particle surface, indicating while the P-LXMO particle have uniform layered lattice ordering from the bulk up to surface, ASR-LXMO has a dense spinel shell at the particle surface.



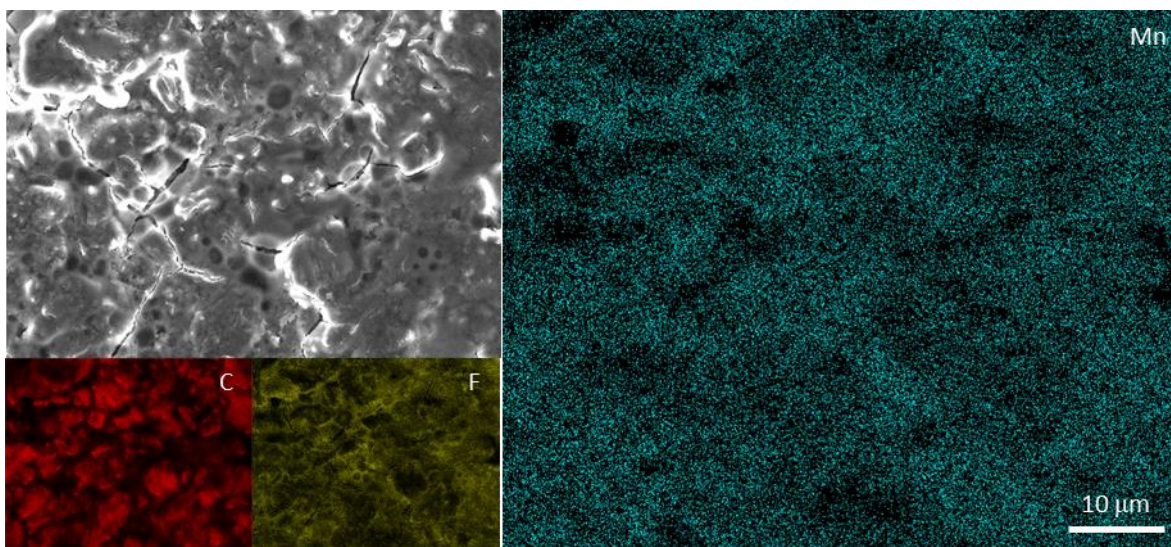
Supplementary Figure 3 The rates cycling of P-LXMO and ASR-LXMO cathodes



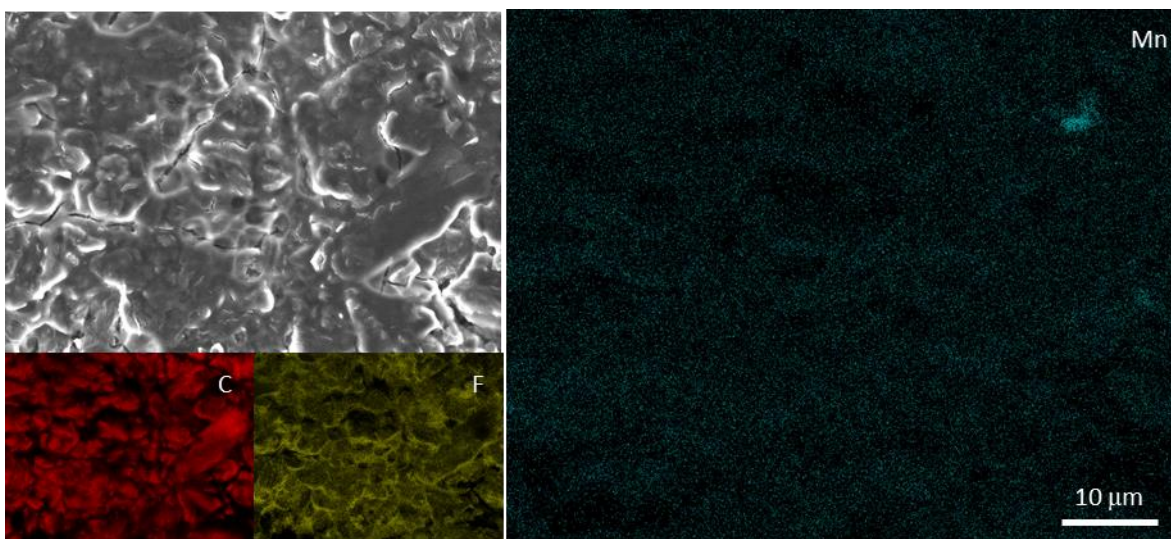
Supplementary Figure 4 Quantitative fitting of the iFY sXAS Mn L-edges of P-LXMO (a) and ASR-LXMO (b) at discharge states in different cycles, by a linear fitting with standard references of MnO, Mn₂O₃ and MnO₂. The results were summarized in Supplementary Table 3.



Supplementary Figure 5 The iFY sXAS Ni L-edge of the P-LXMO (a) and ASR-LXMO (b) particle in different cycles. All the Ni L-edges at discharge states indicated that the Ni ions kept in +2 valence in both the two materials cycling, while all the Ni L-edges at charged states also changed little in cycling. Therefore, we can roughly infer that Ni contributed constant capacity in cycling. Because of the absence of standard Ni⁴⁺ L-edge for reference, we cannot quantify the Ni valence at charge state. So in this work, we assume all Ni ions can be charged to +4 in the cycling, and estimate that Ni contributed 0.4e and 126.1 mAh/g in each cycle.



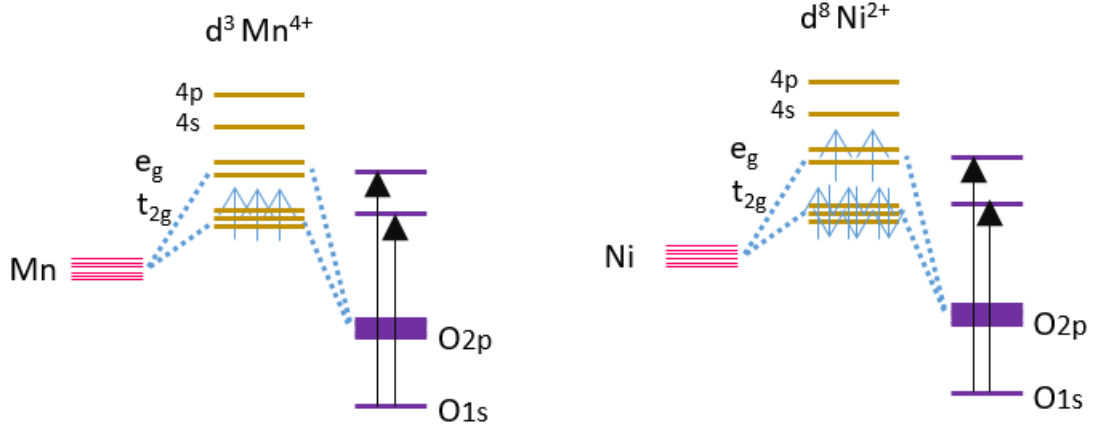
Supplementary Figure 6 EDX mapping of the graphite anodes after 200 cycles, disassembled from the pouch full-cell with P-LXMO cathode to show the C (red), F (yellow) and Mn (green) composition and distribution at the graphite anode.



Supplementary Figure 7 EDX mapping of the graphite anodes after 200 cycles, disassembled from the pouch full-cell with ASR-LXMO cathode to show the C (red), F (yellow) and Mn (green) composition and distribution at the graphite anode.

Supplementary note 1

Quantitative analysis of the electrons extracted in the charge process by sXAS O K-edge



Schematic diagrams of XAS transitions from O1s to the holes on each transition metal²

The integral of the O K edge XAS for $\text{Li}_{1.20}[\text{Ni}^{2+}_{0.2}\text{Mn}^{4+}_{0.6}]\text{O}_2$ material during charging can be used to indicate the number of electrons removed from both M_{3d} and O_{2p} (holes created) orbitals in the charge process, since $\text{O}_{1s} \rightarrow \text{holes}$ transition probability is proportional to the number of holes on M_{3d} and O_{2p} . Because all M ions are hybridized with O in the material, any electron escaped from M or O can be reflected from the O K-edge. The schematic diagrams above show the hybridized M_{3d} and O_{2p} states, which leads to the O K edge XAS peaks at 530 eV (t_{2g} and up-spin on e_g) and 532 eV (down-spin on e_g). For $\text{Mn}^{4+}\text{-O}$, there are 3 holes on t_{2g} and 4 holes on e_g so that there are 7 possible XAS transitions associated with Mn-O, for $\text{Ni}^{2+}\text{-O}$, there are 2 average holes on e_g , and none on t_{2g} . Thus for $\text{Li}_{1.20}[\text{Ni}^{2+}_{0.2}\text{Mn}^{4+}_{0.6}]\text{O}_2$, there can be 4.6 ($=0.6 \times 7 + 0.2 \times 2$) possible XAS transitions in total from O_{1s} . After charge, partial electrons from M_{3d} or O_{2p} were removed, so that there can be more holes generated, and resulted in an enlarged O K edge XAS peaks at 530 eV and 532 eV. If the integral of O pre K edge after charged was $a \times (a > 1)$ that of the discharged states, then the average number of holes (δ^+) in the bulk per formula unit should satisfy $4.6 + \delta^+ = 4.6 \times a$. So

$$\delta^+ = 4.6(a - 1)$$

and δ^+ can be the total number of removed electrons from both M and O ions, which contribute to the charged capacity.

Similarly, for the spinel $\text{LiMn}_{1.5}\text{Ni}_{0.5}\text{O}_4$ surface, Mn owns 1.5×7 holes, and Ni owns 0.5×2 holes, so the overall number of holes from the spinel surface can be estimated by

$$\delta^+ = 11.5(a - 1).$$

From Fig. 4b, the integration of O K edge TEY sXAS peaks at 527.5 eV-534.2 eV after charge of P-LXMO was $a = 1.220$ times to that of the discharged states, so we can calculate $\delta^+ = \sim 1.01$ (318 mAh/g) was initially charged from the surface of P-LXMO particle. However, based on the integral change of TEY O K-edge XAS peaks of ASR-LXMO ($a = 1.083$), we can get that only $\delta^+ = \sim 0.95$ (141 mAh/g) is initially charged from the ASR-LXMO surface.

Supplementary Table 1 ICP-AES results for P-LXMO and ASR-LXMO samples. The ICP result indicates that the Li content was reduced from 1.226 to 1.167 after ASR, while Mn and Ni kept unchanged. The decreased $\Delta\text{Li} = -0.059$ (1.167-1.226) was exactly double the amount of MoO_3 used

(0.0297, 5 wt%). Therefore, all MoO₃ has transformed to Li₂MoO₄ after leaching. After washing with water, this Li₂MoO₄ layer is totally removed, as there was none Mo detectable in ASR-LXMO.

	P-LXMO			ASR-LXMO			
	Li	Mn	Ni	Li	Mn	Ni	Mo
1	1.226	0.603	0.197	1.169	0.604	0.196	<0.0001
2	1.227	0.601	0.199	1.166	0.601	0.199	<0.0001
3	1.224	0.603	0.197	1.165	0.602	0.198	<0.0001
	1.226	0.603	0.197	1.167	0.602	0.198	<0.0001

Supplementary Table 2 Refined lattice parameters and refinement parameters of the phases

Phase	Percentage /wt%	a /Å	b /Å	c /Å	α /°	β /°	γ /°	R _{wp} /%
<i>C2/m</i>	93.9	4.9579	8.5837	5.0321	90	109.108	90	6.65
<i>Fd3m</i>	6.1	8.4252	8.4252	8.4252	90	90	90	11.27

Refined crystallographic parameters

Space group: *C2/m*

Atom	site	x	y	z	Occupancy
Li	2b	0	0.500	0	0.409
Ni	2b	0	0.500	0	0.210
Mn	2b	0	0.5	0	0.379
Li	2c	0	0	0.500	1
Li	4h	0	0.695	0.500	0.945
Ni	4h	0	0.695	0.500	0.055
Mn	4g	0	0.167	0	0.709
Li	4g	0	0.170	0	0.151
Ni	4g	0	0.170	0	0.139
O1	4i	0.224	0	0.224	1
O2	8j	0.251	0.332	0.234	1

Space group: *Fd3m*

Atom	site	x	y	z	Occupancy
Li	8a	0.125	0.125	0.125	0.983
Mn	8a	0.125	0.125	0.125	0.015
Li	16d	0.500	0.500	0.500	0.062
Ni	16d	0.500	0.500	0.500	0.241
Mn	16d	0.500	0.500	0.500	0.697
O	32e	0.265	0.500	0.500	1

Supplementary Table 3 The valences of Mn at discharge states in different cycles in P-LXMO and ASR-LXMO, by a quantitative analysis of sXAS Mn L₃ edges in Supplementary Fig. 2, and the capacity contribution when charged to Mn⁴⁺.

Cycle	P-LXMO	ASR-LXMO
-------	--------	----------

	Mn	Capacity [mAh/g]	Mn	Capacity [mAh/g]
2 nd	+3.96	7.6	+3.98	3.8
100 th	+3.78	41.6	+3.94	11.4
200 th	+3.65	66.2	+3.92	15.1

Supplementary Table 4 Charged capacity from the quantitative analysis of FY sXAS O-K edges of the two materials in different cycles based on $\delta^+=4.6(a-1)$, as discussed in Supplementary Note 1, and the capacity were calculated from $C=26.8\delta^+/M$, $M=85$.

Cycle	P-LXMO	ASR-LXMO
	Capacity [mAh/g]	Capacity [mAh/g]
2 nd	240.1	238.2
100 th	232.3	240.1
200 th	219.3	235.9

Supplementary Table 5 The content of Mn at the graphite anodes disassembled from the pouch full-cells after 200 cycles. Three parts (each was 1 cm³) were measured with ICP-AES for each graphite foil that was all immersed in 65% HNO₃ solution for 7 days.

	P-LXMO	ASR-LXMO
	Mn [$\mu\text{g}/\text{cm}^2$]	Mn [$\mu\text{g}/\text{cm}^2$]
1	99.2	31.5
2	94.7	22.6
3	102.1	25.7
Average	98.7	26.6

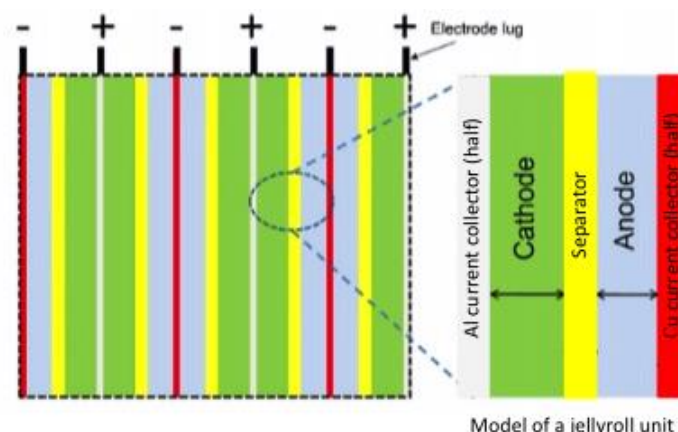
Supplementary discussion 1

We used the following equations to estimate the gravimetric and volumetric energy density of the jellyroll full cell (excluding the Al-plastic cover) [*Joule*, 4 (2020): 539-554]:

$$E_g = E/m_{\text{cell}}$$

$$E_v = E/V_{\text{cell}}$$

To simplify the process, we can roughly estimate the weight (m_{cell}) and volume (V_{cell}) of a pouch full-cell with a sandwich-structure model [*Current Opinion in Electrochemistry*, 6 (2017): 92-99]. Regarding the thicknesses of the current collectors, we use half of the thicknesses of the foils in this model due to the widely used double-side coating technology industrially.



If we ignore the slight larger area of separator used than electrodes, the weight (m_{unit}) and volume (V_{unit}) of one jellyroll unit can be calculated (excluding electrolyte) by

$$m_{\text{unit}} = \frac{1}{2} m_{\text{Al current collector}} + m_{\text{cathode}} + m_{\text{separator}} + m_{\text{anode}} + \frac{1}{2} m_{\text{Cu current collector}}$$

$$= A * (\frac{1}{2} L_{\text{Al current collector}} + L_{\text{cathode}} + L_{\text{separator}} + L_{\text{anode}} + \frac{1}{2} L_{\text{Cu current collector}});$$

$$V_{\text{unit}} = A * (\frac{1}{2} d_{\text{Al current collector}} + d_{\text{cathode}} + d_{\text{separator}} + d_{\text{anode}} + \frac{1}{2} d_{\text{Cu current collector}})$$

where A is the electrodes area, L is the areal density (g/cm^2) and d is the thickness. Therefore, the weight and volume of the full-cell can be calculated by (with an even n)

$$m_{\text{cell}} = n m_{\text{unit}} + A * L_{\text{Al current collector}} + m_{\text{cathode tab}} + m_{\text{anode tab}} + m_{\text{electrolyte}}$$

$$V_{\text{cell}} = n V_{\text{unit}} + A * d_{\text{Al current collector}}$$

where n is the number of units fabricated in the cell.

In the full-cell fabrication process, we used the parameters listed in the table below and obtained a pouch full-cell with 99 mAh, 351 mWh. According to the above equations, the weight energy density of the pouch full-cell can be calculated as 249 Wh/kg, while the volumetric energy density of the pouch full-cell can be calculated as 782 Wh/L. Please note, we only used two units ($n=2$) in the full-cell, so with a higher n (like $n=20$ that always used in industrial fabrication), we can further improve the above values to 280 Wh/kg and 812 Wh/L.

A	15.7 cm^2
n	2
$L_{\text{Al current collector}}$	3.24 mg/cm^2
$L_{\text{separator}}$	0.8 mg/cm^2
$L_{\text{Cu current collector}}$	8.06 mg/cm^2
L_{cathode}	13.9 mg/cm^2
L_{anode}	12 mg/cm^2
$d_{\text{Al current collector}}$	12 μm
$d_{\text{Cu current collector}}$	9 μm
d_{cathode}	46.5 μm
d_{anode}	68 μm
$d_{\text{separator}}$	12 μm
$m_{\text{Al cathode tab}}$	32 mg
$m_{\text{Ni anode tab}}$	94 mg
$m_{\text{electrolyte}}$	242 mg

If we fabricate a pouch full cell with LCO(4.4V) and Ni-rich(811) cathodes for the same capacity (3.5 mAh/ cm^2), we can get the mass and volumetric energy density in the following table. It is clear that the ASR-LXMO cathode has the highest mass energy density among the three cathodes, and most importantly, LXMO has the lowest material cost as it was free of Co and only used small amount of Ni, so which would have the lowest cost ($\$/\text{kWh}$).

	Mass energy density [Wh/kg]		Volumetric energy density [Wh/L]	
	$n=2$	$n=20$	$n=2$	$n=20$
ASR-LXMO	249	280	782	812
LCO(4.4V)	232	259	815	846
Ni-rich(811)	243	272	803	835

References

- 1 Liebertz, J. & Rooymans, C. Phase behaviour of Li_2MoO_4 at high pressures and temperatures. *Solid State Communications* **5**, 405-409 (1967).
- 2 Luo, K. *et al.* Charge-compensation in 3d-transition-metal-oxide intercalation cathodes through the generation of localized electron holes on oxygen. *Nat Chem* **8**, 684-691, doi:10.1038/Nchem.2471 (2016).